In-situ U-Pb dating of Ries Crater lacustrine carbonates (Miocene, South-West Germany): implications for continental carbonate chronostratigraphy

Damaris Montano (damaris.montano@ifpen.fr)[1,2,3,4]; Marta Gasparrini (marta.gasparrini@unimi.it)[1,5]; Axel Gerdes (gerdes@em.uni-frankfurt.de)[2,3]; Giovanna Della Porta (giovanna.dellaporta@unimi.it)[5]; Richard Albert[2,3] (AlbertRoper@em.uni-frankfurt.de)[2,3].

(1) IFP Energies nouvelles, 1-4 avenue de Bois-Préau, 92852, Rueil-Malmaison (France).

(2) Institut für Geowissenschaften, Goethe University Frankfurt, Altenhöferallee 1, 60438 Frankfurt am Main (Germany).

(3) Frankfurt Isotope and Element Research Center (FIERCE), Goethe University Frankfurt, Frankfurt am Main (Germany).

(4) Sorbonne Université; ED 398 – GRNE, 4, place Jussieu, 75252 Paris (France).

(5) Università degli Studi di Milano; Dipartimento di Scienze della Terra "Ardito Desio", via Mangiagalli 34, 20133 Milan (Italy).

Abstract

The Nördlinger Ries Crater lacustrine basin (South-West Germany), formed by a meteorite impact in the Miocene (Langhian; ~14.9Ma), offers a well-established geological framework to understand the strengths and limitations of U-Pb LA-ICPMS (*in situ* Laser Ablation-Inductively Coupled Plasma Mass Spectrometry) geochronology as chronostratigraphic tool for lacustrine (and more broadly continental) carbonates. The post-impact deposits include siliciclastic basinal facies at the lake centre and carbonate facies at the lake margins, coevally deposited in a time window of >1.2 and <2Ma. Depositional and diagenetic carbonate phases (micrites and calcite cements) were investigated from three marginal carbonate facies (Hainsfarth bioherm, Adlersberg bioherm and Wallerstein mound). Petrography combined with C and O stable isotope analyses indicate that most depositional and early diagenetic carbonates preserved pristine geochemical compositions and thus the U-Pb system should reflect the timing of original precipitation. In total, 22 U-Pb ages were obtained on 10 different carbonate phases from five samples. The reproducibility and accuracy of the U-Pb (LA-ICPMS) method were estimated to be down to 1.5% based on repeated analyses of a secondary standard (speleothem calcite ASH-15d) and propagated to the obtained ages. Micrites from the Hainsfarth, Adlersberg and Wallerstein facies yielded ages of 13.90±0.25, 14.14±0.20 and 14.33±0.27Ma, respectively, which overlap within uncertainties, and are consistent with the weighted average age of 14.30±0.20Ma obtained from all the preserved depositional and early diagenetic phases. Data indicate that sedimentation started shortly after the impact and persisted for >1.2 and <2Ma, in agreement with previous constraints from literature, therefore validating the accuracy of the applied method. Later calcite cements were dated at 13.2±1.1 (n_w=2), 10.2±2.7 and 9.51±0.77Ma, implying multiple post-depositional fluid events. This study demonstrates the great potential of the U-Pb method for chronostratigraphy in continental systems, where correlations between time-equivalent lateral facies are often out of reach. In Miocene deposits the method yields a time resolution within the 3rd order depositional sequences (0.5-5Ma).

Keywords: U-Pb dating, Laser Ablation, lacustrine carbonates, chronostratigraphy, Miocene.

1. Introduction

The application of carbonate U-Pb geochronology was initially limited mainly due to the difficulty in identifying carbonate samples with high and variable U/Pb isotope ratios, together with the analytical challenge in handling low amounts of U and Pb (usually <1ppm) heterogeneously incorporated in carbonates (Rasbury and Cole, 2009). Analytical advances in *in-situ* U-Pb geochronology via Laser Ablation-Inductively Coupled Plasma Mass Spectrometry (LA-ICPMS) have greatly facilitated direct dating of carbonates (e.g. Roberts et al., 2017; 2020; Guillong et al., 2020).

Recent carbonate U-Pb geochronology studies have focussed on a wide spectrum of applications within the geosciences, including the assessment of tectonic events and fracturing (e.g. Hansman et al., 2018; Nuriel et al., 2019), the thermal evolution of sedimentary basins (e.g. Mangenot et al., 2018; MacDonald et al., 2019) and fluid-rock interactions (e.g. Li et al., 2014; Godeau et al., 2018). Previous studies showed that carbonate geochronology via U-Pb (LA-ICPMS) often produces ages that exceed 2-3% precision (2σ) (Roberts et al., 2020), making the technique not always suitable for stratigraphic applications. The U-Pb (LA-ICPMS) geochronology has been used to determine carbonate depositional ages by dating speleothems and palaeosoils (e.g. Scardia et al., 2019; Kurumada et al., 2020) and only a few studies have reported U-Pb ages for lacustrine carbonates (e.g. Cole et al., 2005; Frisch et al., 2019).

Furthermore, to our best knowledge, no study has attempted chronostratigraphic reconstructions for continental carbonates deposited in time windows of < 5Ma.

Dating lacustrine carbonates is relevant for a variety of applications. In particular, these deposits may assist palaeoenvironmental and palaeoclimatic studies since they potentially record the lake geochemical evolution through time. Moreover, they represent potential sources and reservoirs for hydrocarbons and are targets for petroleum exploration (e.g. Bohacs et al., 2000; Rohais et al., 2019). Lacustrine marginal carbonates include coated grain and skeletal carbonate sands, as well as carbonate build-ups, which are typically located along the lake shoreline and often organized in discontinuous bodies (e.g. Della Porta, 2015 and references therein). They are characterized by high facies heterogeneity and commonly lack biostratigraphic markers, which hinders chronostratigraphic correlations among time-equivalent lateral facies (e.g. Deschamps et al., 2020). Furthermore, the site-specific geochemistry of continental fluids does not permit the use of proxies, such as $\delta^{18}O$, $\delta^{13}C$ and $^{87}Sr/^{86}Sr$, conventionally applied to indirectly date marine carbonates by correlating with global chemostratigraphic curves (Veizer et al., 1999). Consequently, at present, constraining the relative and absolute ages of lacustrine marginal carbonates and performing basin-scale correlations remain a challenge.

The Miocene Nördlinger Ries Crater in South-West Germany is one of the most precisely dated meteorite impact basins on Earth. The impact timing has been constrained by the U-Pb and Ar-Ar geochronometers (Schwarz et al., 2020 and references therein). The post-impact lacustrine deposits include siliciclastic basinal facies and carbonate marginal facies (Füchtbauer et al.,1977; Jankowski,1977). The onset of lacustrine sedimentation is thought to have occurred shortly after the impact (Buchner and Schmieder, 2009; Stöffler et al., 2013) and a magnetostratigraphy dataset is available for the basinal facies (Pohl, 1977; Pohl et al., 2010).

Different depositional and diagenetic carbonate phases (i.e. micrites and calcite cements) from three marginal facies of the Ries Crater basin were investigated with conventional petrography and carbon (C) and oxygen (O) stable isotope analyses prior to U-Pb geochronology. This was aimed at identifying phases not affected by later diagenetic modifications, which could have reset the carbonate U-Pb system (Li et al., 2014; Mangenot et al., 2018).

This study aims to assess: (1) the reliability of the U-Pb (LA-ICPMS) method to obtain geologically consistent (i.e. accurate) and precise ages from lacustrine carbonates of known stratigraphic age (Miocene) deposited in a time window of <2 Ma; and (2) the suitability of this method for chronostratigraphy and diagenesis studies in continental sedimentary settings.

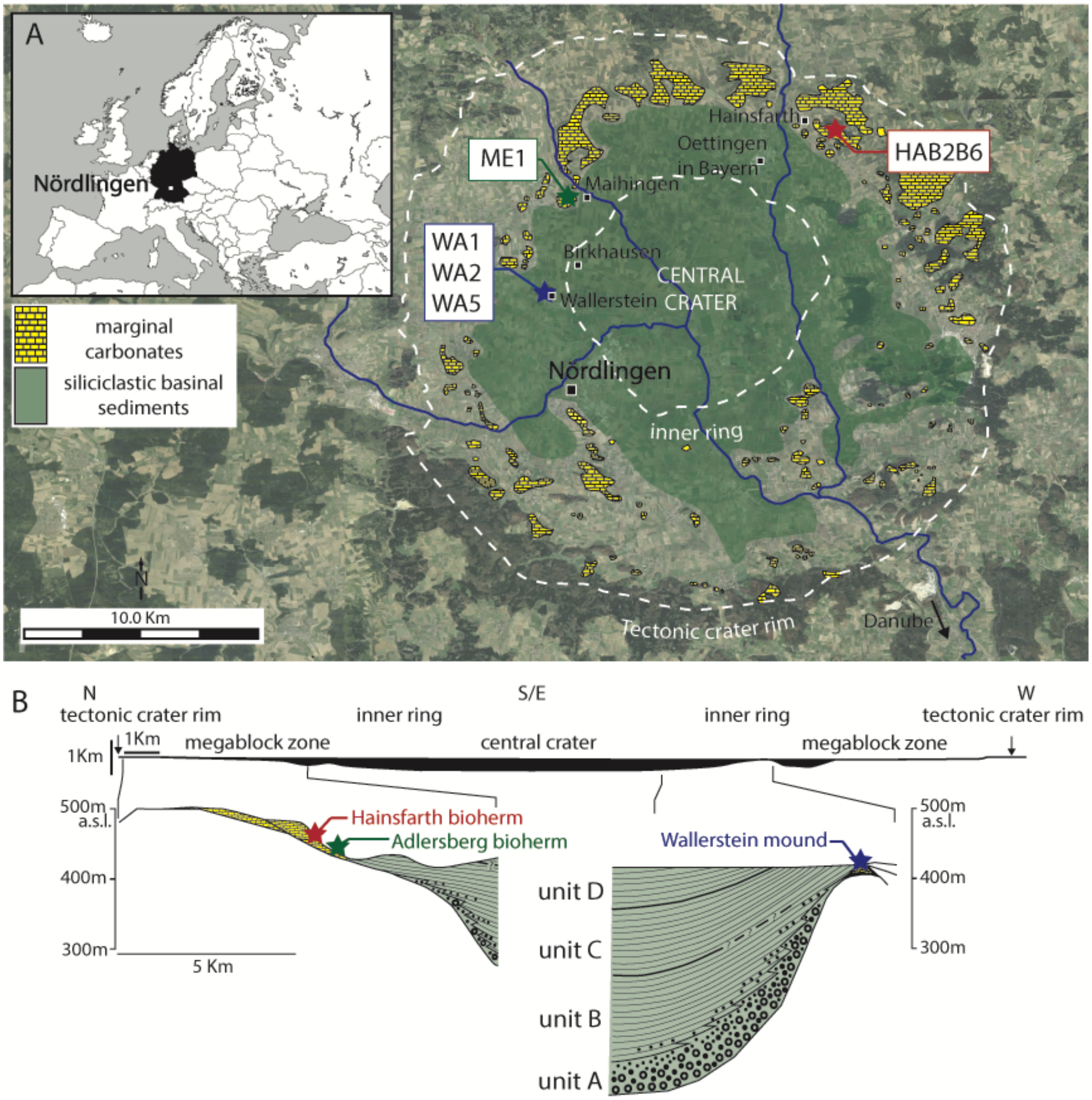

Figure 1. Geographic and geological setting of the study area. **A)** In the insert, the location of the Ries Crater impact lake in South-West Germany (centred at 48° 52′ 5.3" N, 10° 33 ′ 32" E). The *Google Earth* satellite image illustrates the main structural elements of the impact zone and the location of basinal and marginal deposits. The provenance of the investigated samples (HAB2B6, ME1, WA1, WA2 and WA5) is also reported. **B)** Simplified North–South cross-section of the Ries

Crater (modified after Arp et al., 2013a). On the left, the location of the studied carbonate marginal facies (Hainsfarth bioherm, Adlersberg bioherm, and Wallerstein mound) is indicated by stars. On the right are reported the basinal A-B-C-D lithostratigraphic units that correspond respectively to the basal, the laminite, the marlstone and the claystone members (after Füchtbauer et al., 1977; Jankowski, 1977).

2. Geological and geochronological setting

The Nördlinger Ries lacustrine basin is a circular, flat depression of ~26km in diameter located in South-West Germany (Fig. 1) that formed due to a meteorite impact (Shoemaker and Chao, 1961). The impact structure comprises a central crater, an inner ring, a megablock zone and a tectonic crater rim (Füchtbauer et al., 1977) (Fig. 1).

In this study, it is assumed that the meteorite impact occurred at ~14.9Ma (Langhian, Miocene) in line with most ages published in the last decade: 14.92±0.02Ma (Rocholl et al., 2018), 14.808±0.038 Ma (Schmieder et al. 2018a), 14.89±0.34 and 14.75±0.22Ma (Schwarz et al., 2020) (see details in Data repository A).

Shortly after the impact, a fluvial system was established within the crater (Jankowski, 1981; Buchner and Schmieder, 2009; Stöffler et al., 2013). River waters, along with post-impact springs circulated in the basin forming the Ries Crater lake. By the end of the Miocene the basin was filled by up to 350m of lacustrine sediments (Bolten & Müller, 1969; Arp et al., 2017).

The Ries post-impact sedimentary succession was investigated through outcrop surveys and borehole core drillings (Füchtbauer et al., 1977; Jankowski, 1977; Arp et al., 2013a, b; 2017;

2019) and comprises a basinal succession at the lake centre and marginal facies on the lake margins (Fig. 1).

The basinal succession was subdivided into four lithostratigraphic units (Füchtbauer et al., 1977; Jankowski, 1977) from base to top (Fig. 1): basal member (unit A) mainly consisting of sandstones reworked from suevite (Stöffler et al., 2013); laminite member (unit B); marlstone member (unit C); and claystone member (unit D), partially eroded during Plio-Pleistocene time.

Four main facies characterize the basin margins (Arp, 1995 and references therein) (Fig. 1): algal bioherms, sub-lacustrine spring mounds, carbonate sands and fluvio-deltaic conglomerates. Algal bioherms (i.e. Staudiberg, Hainsfarth and Adlersberg; Arp, 1995) are mainly built by inverted cones of *Cladophorites* green algae, encrusted by micrite (Riding, 1979; Arp, 1995; Della Porta, 2015). Spring mounds are associated with post-impact hydrothermal springs (e.g. Erbisberg mound; Arp et al., 2013b) or ambient temperature springs (e.g. the Wallerstein mound; Pache et al., 2001) discharging into the lake, and consist of mounds and pinnacles made of porous crystalline, micritic laminated and clotted peloidal carbonate fabrics (Arp, 1995; Pache et al., 2001).

A precise time estimate for the duration of lacustrine sedimentation remains hard to define because the uppermost deposits of basinal unit D have been eroded during Plio-Pleistocene time (Füchtbauer et al., 1977). Based on rhythmic laminations and magnetostratigraphic data from basinal sediments, Füchtbauer et al. (1977) and Pohl (1977) proposed that the entire (preserved and eroded) lacustrine succession was deposited over a time window of 0.3 to 2Ma, whereas more recently, Arp et al. (2017) reported a duration of 2Ma. Additionally, based on sedimentation rates of basinal units, Jankowski (1981) suggested that the currently preserved

lacustrine deposits formed over a time interval of up to 1.2Ma. Thus, according to the existing literature constraints, the four (A-B-C-D) basinal units were deposited in a time window of >1.2 and <2Ma. Further age constraints on the deposition of the basinal units derive from magnetostratigraphy data (Pohl 1977; Pohl et al., 2010), using an approach previously presented by Arp et al. (2013b). In this contribution the meteorite impact was assigned to the top of C5Bn.1r reverse chron in line with the interpretation of Rocholl et al. (2017, 2018). As a consequence, unit A is considered to be deposited during the C5Bn.1n normal chron, the transition from unit B to unit C is within the C5Adr chron and the onset of unit D deposition was assigned to the boundary between C5ACr and C5ACn chrons (see details in Data repository A).
The duration inferred from magnetostratigraphic data agree with the one previously established via sedimentological and stratigraphic studies (Füchtbauer et al., 1977; Pohl, 1977).

3. *Material and methods*

3.1 Investigated samples

Five microbial boundstone samples from the marginal facies of the Ries Crater were collected from three locations (Fig. 1 and Table 1). The HAB2B6 sample (Hainsfarth bioherm facies) and the ME1 sample (Adlersberg bioherm facies) come from the Hainsfarth quarry and the Mellerberg locality, respectively (see Arp, 1995). The WA1, WA2 and WA5 samples (Wallerstein mound build-up facies) were collected at the base of the Wallerstein Castle (see Pache et al., 2001). Although the sample stratigraphic height along the Wallerstein mound is unknown, based on the petrographic description of Pache et al. (2001), WA1 and WA2 can be ascribed to the basal part of the mound, and WA5 to the central part.

Sample name	Sample location	Facies	Microfacies	Carbonate phases
HAB2B6	Hainsfarth quarry 48°57’09.2"N; 10°38’33"E	Hainsfarth *Cladophorites* green algae bioherm located at the lake margin	Peloidal skeletal packstone and algal microbial boundstone with *Cladophorites* green algae tubes and ostracods, gastropods (e.g. *Hydrobia trochulus* Sandberger), bivalves. Bioclasts are encrusted by leiolitic micrite. Primary, mouldic and vuggy pores are partially filled by cements.	MIC-H micrite; BL and BM cements
ME1	Mellerberg 48°55’22.5"N; 10°29’32"E	Adlersberg *Cladophorites* green algae bioherm located at the lake margin	Algal microbial boundstone consisting of *Cladophorites* green algae stems encrusted by leiolitic and clotted peloidal micrite. Primary framework pores are locally filled by ostracods and bivalve peloidal packstone/grainstone. Primary, mouldic and vuggy pores are partially filled by cements.	MIC-A micrite; DOL, B1, B2 and B3 cements
WA1, WA2	Wallerstein Castle 48°53’20.85"N; 10°28’27.4"E	Wallerstein sub-lacustrine spring mound, located at the lake margin at the site of groundwater spring	Lenticular undulated or planar rigid framework made of irregular mm-thick layers of leiolitic to clotted peloidal micrite. Primary and vuggy pores are partially filled by cements.	MIC-M micrite; M2 and M3 cements
WA5			Framework of globose pendant-like calcite cements selectively affected by silicification (chalcedony sphaeroids). Clusters of micrite with leiolitic to clotted peloidal fabric. Primary and vuggy pores are partially filled by cements.	MIC-M micrite; M1, M2 and M3 cements

Table 1. Location, facies description and depositional environment of the five samples investigated. Macro- and microscopic facies are based on previous studies by Riding (1979), Arp

(1995) and Della Porta (2015). The carbonate phases occurring in each sample are also reported (see details in Table 2).

3.2 Petrographic analysis

Eight polished thin sections (50-60μm thick) were prepared in order to identify the different depositional and diagenetic carbonate phases (Table 2). Conventional optical petrography was performed using a Nikon ECLIPSE LV100POL polarized light microscope under plane- and cross-polarized light (PPL and XPL). Cathodoluminescence (CL) microscopy was accomplished with a cold CL 8200 Mk5 CITL instrument. The electron beam worked under vacuum (<0.1 mbar) with an acceleration voltage of 10kV and a current of 250μA. All thin sections were partially stained with a solution of 10% diluted HCl, Alizarin red-S and potassium ferricyanide (Dickson, 1966).

Facies	Carbonate phase	Petrographic description	Staining	Cathodoluminescence (CL) response	Post-depositional diagenetic modifications
Hainsfarth bioherm	MIC-H	Leiolitic to clotted peloidal micrite (Fig. 2A). Crystal size < 4µm.	Pink	Dull to bright orange	No
	BL	Isopachous crusts of fibrous calcite cement, 80 µm in thickness (Fig. 2A), lining the clotted peloidal microbial framework pores.	Pink	Dark orange to red	No
	BM	Blocky calcite consisting of limpid-transparent crystals, 50 to 1000µm in size (Fig. 2A)	Pink	Two luminescence domains: BMa is non-luminescent and terminates with a ~10µm thick bright orange zone; BMb is non-luminescent (Fig. 2A)	No
Adlersberg bioherm	MIC-A	Leiolitic to clotted peloidal micrite (Fig. 2B,C,D). Crystal size < 4µm.	Pink with unstained areas (Fig. 2C)	Mottled. Non-luminescent to dull red (Fig.3D)	Minor dissolution and recrystallization. Local replacement by microcrystalline dolomite (Fig. 2C)
	B1	Pendant calcite cement, up to 150 µm in size. Crystals are inclusion-rich and light brown in PPL (Fig. 2B)	Pink	Non-luminescent to dull orange	No
	DOL	Isopachous rim of dolomite cement, 50 µm in thickness (Fig. 2B,C,D)	Unstained (Fig. 2C)	Non-luminescent to very dull red (Fig. 2D)	No
	B2	Isopachous rim of dogtooth to bladed calcite cement, 200µm in thickness. Crystals are limpid in PPL (Fig. 2B,C,D)	Pink (Fig. 2C)	Zoned. Usually dull red crystal cores with bright orange overgrowths (Fig. 2D)	No
	B3	Blocky (ferroan) calcite cement, locally with drusy fabric. Crystals are limpid in PPL and up to 100 µm in size (Fig. 2 B,C,D).	Blue (Fig. 2C)	Dull orange (Fig. 2D)	No
Wallerstein mound	MIC-M	Leiolitic to clotted peloidal micrite (Fig. 2E,F) planar to wavy laminae forming a porous framework. Crystal size < 4µm.	Pink	Dull orange	Local dissolution and rare silicification (chalcedony)
	M1	Globose pendant cement with coalescent calcite crystals, up to 500µm in size, with sweeping extinction in CPL (Fig. 2G). Alternation of inclusion-rich and inclusions-free zones in PPL.	Pink (Fig. 2E,G)	Non-luminescent to dull orange. Locally with bright to dull orange zones (Fig. 2H)	Minor silicification (chalcedony) (Fig. 2G)
	M2	Isopachous rims of fibrous calcite cement, 500µm in thickness (Fig. 2E,F,G,H)	Pink (Fig. 2G)	Zoned. From bright/dull orange to non-luminescent	Dissolution at the M1 and M2 boundary (Fig. 2G,H)
	M3	Blocky calcite cement. Crystals are limpid and up to 500 µm in size (Fig. 2E,F,G,H)	Pink (Fig. 2E)	Very bright orange (Fig. 2F)	No
	SIL	Chalcedony sphaeroids, ~ 250µm in size, with sweeping extinction (Fig. 2G), selectively replacing M1 cores and portions of MIC-M.	Unstained (Fig. 2E)	Non-luminescent	No

Table 2. Petrographic description of the phases identified in the three carbonate facies investigated.

3.3 C and O stable isotope analysis

Forty-one powder samples from 10 carbonate phases were carefully extracted from polished rock slabs and thin sections by means of a dental drill or a software-controlled MicroMill device. Powders were reacted with 100% phosphoric acid at 70°C using a Gasbench II connected to a ThermoFisher Delta V Plus mass spectrometer and analysed for C and O stable isotopes at Geozentrum Nordbayern (Germany). $\delta^{13}C$ and $\delta^{18}O$ values for carbonates are reported in ‰ relative to the Vienna Pee Dee Belemnite (V-PDB) standard. Reproducibility and accuracy were monitored by replicate analyses of laboratory standards calibrated by assigning $\delta^{13}C$ values of +1.95‰ to NBS19 and -47.30‰ to IAEA-CO9 and $\delta^{18}O$ values of -2.2‰ to NBS19 and -23.2‰ to NBS18. Reproducibility for $\delta^{13}C$ and $\delta^{18}O$ values measured on the studied carbonates was ±0.04 and ±0.03 ‰ (1σ), respectively.

3.4 U-Pb isotope analysis and dating

Five of the eight investigated thin sections were analysed in seven U-Pb LA-ICPMS analytical sessions at the Goethe University of Frankfurt (Germany). Prior to analysis, the sections were cleaned in an ultrasonic bath with ethanol (5% mol/L). Analyses were performed in different analytical sessions between 2016 and 2019 using a Thermo Scientific Element 2 sector field ICP-MS, coupled to a RESOlution (Resonetics) 193 nm ArF Excimer laser (CompexPro 102, Coherent) equipped with a S-155 two-volume ablation cell (Laurin Technic, Australia). During each session the ablation parameters were kept constants for all samples and reference materials. Samples were ablated in a helium atmosphere (300 ml) and mixed in the ablation funnel with argon (1 L) and nitrogen (6-8ml). Analyses were performed with a square ablation spot of 143 to 213µm in width, 8 to 12Hz frequency and fluence of around 2J · cm^{-2}. A manual pre-screening session allowed identifying areas with variable U/Pb and $^{207}Pb/^{206}Pb$ ratios. Raw data were corrected off-line using an in-house Microsoft Excel spreadsheet program (Gerdes and Zeh, 2009). Fractionation of $^{206}Pb/^{238}U$, $^{207}Pb/^{206}Pb$ ratios and the drift during the analytical session were corrected based on repeated analyses of soda-lime glass NIST-SRM 614. WC-1 calcite (Roberts et al., 2017) was used to correct for matrix offsets in U-Pb ratios (5 to 9%) between NIST glass and carbonate. Reported uncertainties for each analysis are quadratic additions of the within run precision, counting statistical uncertainties and the excess of variance (2% and 0.2% for the $^{206}Pb/^{238}U$ and $^{207}Pb/^{206}Pb$, respectively). The excess of variance was calculated from the WC-1 reference material. Final results were plotted on U-Pb Tera-Wasserburg Concordia plots using Isoplot3 (Ludwig, 2012) where ages represent the intersection with the Concordia curve. Regression lines were constrained with 6 to 43 ablations spots (n) for each of the investigated carbonate phases. All uncertainties are reported as 2σ. The speleothem calcite ASH-15D secondary reference material (Mason et al., 2016, Nuriel et al., 2020) was analysed as an unknown during six analytical sessions between 2017 and 2019 (Table 3, Data repository C.1 and G.1) to verify the reproducibility and accuracy of the applied method and to compare the datasets from different LA-sessions. The ages obtained from each session yielded a weighted average age of 2.961±0.037 Ma (MSWD = 1.4), consistent within uncertainty with the ID-TIMS age of ASH-15D (2.965 ± 0.011 Ma, 2σ; Nuriel et al., 2020). The obtained reproducibility between the different sessions is 1.6%. The excess of variance (ε`) obtained from ASH-15D data is 1.45 % (2σ) and was added by quadratic addition to the uncertainties of each lower intercept age of the analysed carbonate phases (Table 3). A 0.34% excess of variance (ε`) for the

$^{207}Pb/^{206}Pb$ y-intercept of the regression line was obtained from the ASH-15D data (weighted mean of 0.8737±0.0014 and MSWD = 2 without ε\`, 0.8737±0.0016 and MSWD = 1 with ε\` of 0.34%) and added by quadratic addition to the y-intercept uncertainty of each analysis (i.e. on the $^{207}Pb/^{206}Pb$ initial ratio).

4. *RESULTS*

4.1 Petrography and C-O stable isotope geochemistry

The microbial boundstone from each of the three carbonate facies investigated (Hainsfarth bioherm, Adlersberg bioherm, Wallerstein mound; Fig. 1) display specific depositional and diagenetic features (Figure 2 and Table 2). Petrographic analysis allowed distinguishing 13 depositional and diagenetic phases (Table 1 and 2; Fig. 2). The depositional carbonate phases consist of leolitic to clotted peloidal micrites, labelled MIC-H, MIC-A and MIC-M from the Hainsfarth bioherm, Adlersberg bioherm and Wallerstein mound, respectively. The diagenetic carbonate phases consist of dolomite cement (DOL), chalcedony (SIL) and calcite cements displaying different habits and fabric: pendant calcites (B1 and M1), isopachous rims of fibrous (BL and M2) and dogtooth to bladed (B2) calcites, as well as blocky calcites (BM, B3 and M3).

The results of the C and O stable isotope analyses for the different carbonate phases sampled are summarized in Figure 3, Table 3 and Data repository B. All micrites (MIC-H, MIC-A, MIC-M) exhibit a covariance between $\delta^{13}C$ and $\delta^{18}O$ (R^2=0.95). $\delta^{13}C$ and $\delta^{18}O$ values for micrites (n=11) range between -5.5‰ and +2.5‰, and between -5.1‰ and +3.3‰, respectively. In particular, MIC-H and MIC-A micrites from the Hainsfarth and Adlersberg bioherm samples, respectively, display positive $\delta^{13}C$ and $\delta^{18}O$ values, whereas MIC-M micrites from the Wallerstein mound sample have negative $\delta^{13}C$ and $\delta^{18}O$ values.

$\delta^{13}C$ and $\delta^{18}O$ for the B1 pendant cement (n=1) are +0.2‰ and -1.7‰, respectively, whereas the B2 isopachous cement (n=1) has $\delta^{13}C$ of +1.5‰ and $\delta^{18}O$ of +0.7‰. The blocky cements from the algal bioherms (BM and B3) have a distinctive C-O isotope composition: BM (n=5) is characterized by negative and consistent $\delta^{13}C$ and $\delta^{18}O$ values with $\delta^{13}C$ between -5.4‰ and -5‰ and $\delta^{18}O$ between -7.3‰ and -7.7‰, whereas B3 (n=3) has a uniform C-O isotope composition with $\delta^{13}C$ between +1.4‰ and +1.9‰, and $\delta^{18}O$ between -5.9‰ to -7.5‰. The $\delta^{13}C$ and $\delta^{18}O$ values of the three calcite cements from the Wallerstein mound samples (M1, M2, M3) are characterized by $\delta^{13}C$ between -1.2‰ and -3.4‰, whereas $\delta^{18}O$ values are more variable, ranging between -0.8‰ and -9.6‰. The $\delta^{18}O$ values fall in three distinct clusters: between -0.8‰ and -4.2‰ for M1 (n=4), between -1.8‰ and -5.0‰ for M2 (n=5) and between -5.7‰ and -9.6‰ for M3 (n=10).

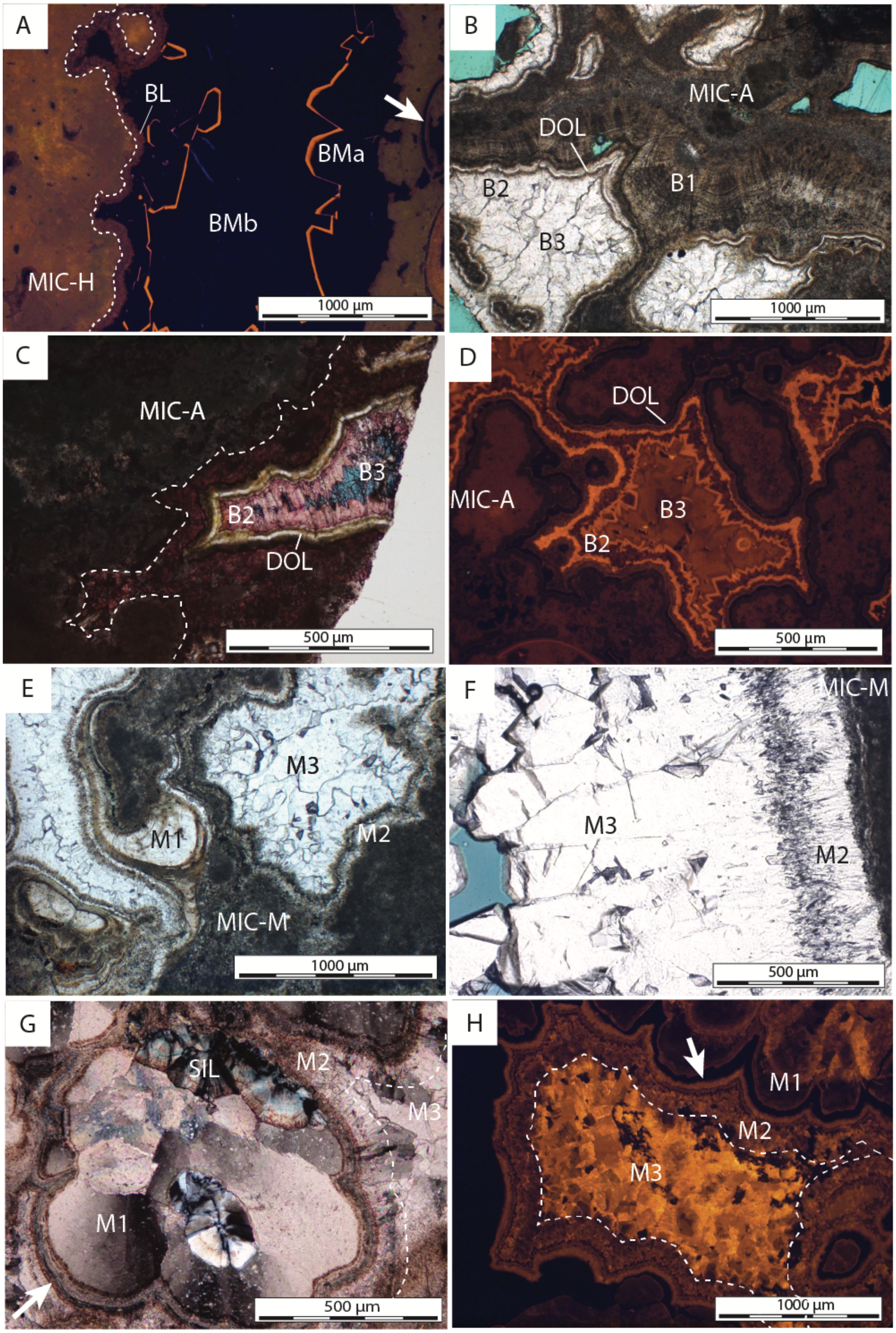
A
BL
BMa
BMb
MIC-H
1000 µm
B
MIC-A
DOL
B2
B1
B3
1000 µm
C
MIC-A
B3
B2
DOL
500 µm
D
DOL
MIC-A
B3
B2
500 µm
E
M3
M1
M2
MIC-M
1000 µm
F
MIC-M
M3
M2
500 µm
G
SIL
M2
M3
M1
500 µm
H
M1
M2
M3
1000 µm

263

Figure 2. Petrographic images of the five carbonate samples investigated. **A)** Microbial boundstone from Hainsfarth algal bioherm composed of clotted peloidal micrite (MIC-H). Primary framework pores are filled by isopachous fibrous calcite (BL) and blocky calcite (BM) cements. BM cement reveals two growth stages (BMa and BMb) under CL. The white arrow indicates a dissolved gastropod shell (mouldic pore). HAB2B6 sample, CL view. **B)** Microbial boundstone from the Adlersberg algal bioherm composed of clotted peloidal micrite (MIC-A). Pores are partially filled by four successive cement phases: pendant calcite (B1), isopachous dolomite rim (DOL), dogtooth to bladed calcite (B2) and blocky calcite (B3). ME1 sample, PPL view. **C)** Microbial boundstone from the Adlersberg algal bioherm composed of clotted peloidal micrite (MIC-A). Primary framework pores are filled by three successive cement generations: isopachous rims of dolomite (DOL) and dogtooth to bladed calcite (B2), followed by a blocky calcite cement (B3). Staining reveals that they consist respectively of non-ferroan dolomite (DOL), non-ferroan calcite (B2) and ferroan calcite (B3). Micrite (MIC-A) is locally replaced by micro-crystalline dolomite (see unstained area to the left of the white dashed line). ME1 sample, stained, PPL view. **D)** Microbial boundstone from the Adlersberg algal bioherm composed of clotted peloidal micrite (MIC-A). Primary framework pores are filled by three successive cement generations: isopachous rims of dolomite (DOL) and dogtooth to bladed calcite (B2), followed by a blocky calcite cement (B3). The micrite (MIC-A) is locally recrystallized as suggested by the mottled CL. ME1 sample, CL view. **E)** Leiolitic to clotted peloidal micrite (MIC-M) from the Wallerstein mound. Primary framework pores are filled by a sequence of three successive cements: globose pendant calcite (M1), isopachous fibrous calcite rim (M2) and blocky calcite (M3). M1 pendant calcite precipitated directly on the micrite laminae (MIC-M)..

WA1 sample, PPL view. **F)** Details of fibrous calcite cement (M2) precipitated on the Wallerstein mound micrite (MIC-M) and followed by blocky calcite cement (M3). WA2 sample, PPL view. **G)** Details of coalescent crystals of pendant calcite cement (M1), partially affected by silicification (SIL; chalcedony sphaeroids) and followed by fibrous calcite (M2) and blocky calcite (M3) cements, grown in optical continuity. Dissolution at the boundary between M1 and M2 cements is indicated by the white arrow. WA5 sample, stained, XPL view. **H)** Globose pendant calcite cement (M1) filling a pore and post-dated by fibrous calcite cement (M2) and blocky calcite cement (M3) with dull red and bright orange luminescence, respectively. Dissolution at the boundary between M1 and M2 cements is pointed by the white arrow. WA5 sample, CL view.

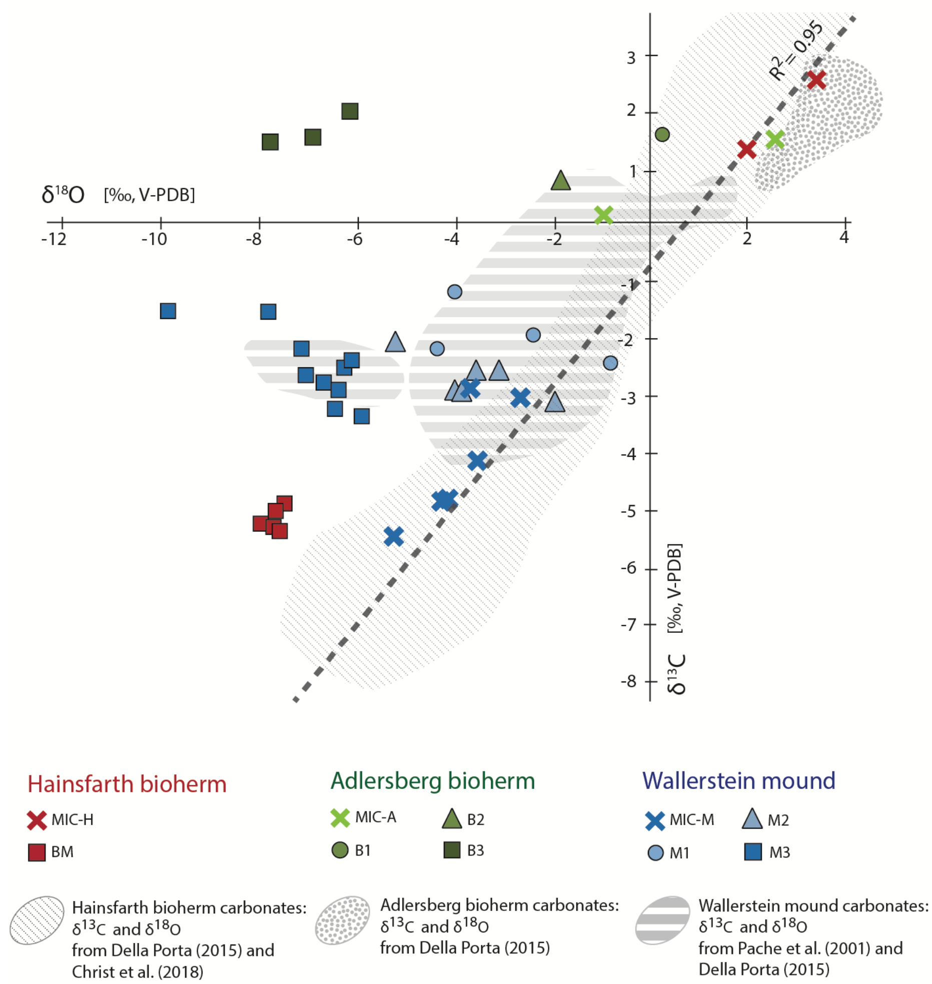

Figure 3. Cross-plot of $\delta^{13}C$ *versus* $\delta^{18}O$ values (in ‰, relative to V-PDB) of the carbonate phases analysed from the three facies investigated. MIC-H, MIC-A and MIC-M stand for micrite from Hainsfarth bioherm, Adlersberg bioherm and Wallerstein mound, respectively. B1 and M1 are pendant calcite cements. B2 and M2 are isopachous calcite cements. BM, B3 and M3 are blocky calcite cements. Note the covariance (R^2=0.95) between $\delta^{13}C$ and $\delta^{18}O$ values that characterizes the micrites (reported as crosses). Grey areas indicate the $\delta^{13}C$ and $\delta^{18}O$ values previously published for the three carbonate facies investigated (Pache et al., 2001; Della Porta, 2015; Christ et al., 2018).

4.2 U-Pb geochronology

The concentrations and isotope ratios of U and Pb of all analysed phases are summarized in Figure 4, Table 3, and Data repository C.1. Due to their small volume, the BL and DOL phases were not sampled and thus not analysed. U and Pb concentrations are very variable, ranging from 10ppb to 53ppm, and 0.4ppb to 6.4ppm, respectively (Fig. 4A). The highest U concentrations can be found in micrites (MIC-H, MIC-A, MIC-M) and pendant cements (B1), mostly with values higher than 1 ppm (Fig. 4A). Figure 4B summarises the $^{238}U/^{206}Pb$ versus $^{207}Pb/^{206}Pb$ ratios of all analysed carbonate phases: $^{238}U/^{206}Pb$ varies from 0.03 to 413 and $^{207}Pb/^{206}Pb$ ranges from 0.87 to 0.10. All phases are characterised by a high to very high isotope ratio variability including domains with high μ-values ($^{238}U/^{204}Pb$) close to the Concordia curve. The Hainsfarth bioherm carbonates display the lowest variability, with $^{238}U/^{206}Pb$ ratios below 1. A clear covariance between both isotope ratios (R^2=0.99; Fig. 4B) suggests that most of the analysed carbonate phases formed at about the same time. However, MIC-A micrite and M1, M3, BM and B3 cements also include younger data points that define a different slope (R^2=0.79).

Tera-Wasserburg Concordia plots with lower intercept ages are displayed in Figures 5 and 6, while the complete data set and plots can be found in Data repositories D, E and F. From the five analysed samples, a total of 22 isochron ages were obtained from 10 depositional and diagenetic carbonate phases (Table 3). Depositional (micrite) and diagenetic (cement) carbonate phases yielded well-defined regression lines with ages between 14.44±0.41 and 9.51±0.77 Ma, and MSWD (Mean Squared Weighted Deviation) of 0.5 to 1.6. The pendant cement (M1) from sample WA5 and the blocky calcite cement (B3) from sample ME1 display more scattered isotope ratios, and consequently higher MSWD (2.1 and 2.3, respectively). The precision obtained for the majority of the ages ranges from 1.3 to 8.6% (internal uncertainty $2\sigma_i$; Table 3) and slightly decreases (1.9 to 8.7%) when the long term excess of variance is added (Table 3). After all propagated uncertainties, 60% of the ages have uncertainties below 5% and 27% (six ages) below 3.5%.

Five carbonate phases (MIC-H, MIC-A, MIC-M, BM and B1) were analysed in multiple sessions to check the reproducibility between sessions and to improve the precision of the ages (Table 3). Weighted average ages for these phases are reported with the number (n_w) of analytical sessions undertaken in brackets. Micrites from samples HAB2B6, ME1, and WA2 were analysed in 3 to 4 sessions, yielding weighted average ages of 13.90±0.25Ma (n_w=4), 14.14±0.20Ma (n_w=3) and 13.79±0.42Ma (n_w=3), respectively, confirming a within-session reproducibility of 1.5-2%. The data also indicate that multiple measurements can improve the precision of the ages by a factor of about 2 to 4, since weighted average ages have uncertainties down to 1.5% (2σ).

Initial $^{207}Pb/^{206}Pb$ ratios (i.e. y-axis intercepts; Table 3) fall between 0.825±0.004 and 0.869±0.023 and display a slight scatter, which can be expressed in a weighted average of 0.838±0.003 (MSWD of 9.9). This value is very similar to that derived from the second stage of Stacey and Kramer (1975) model for 14Ma (0.8366). There is no discernible difference in $^{207}Pb/^{206}Pb$ ratios between different samples or carbonate phases (cements versus micrites).

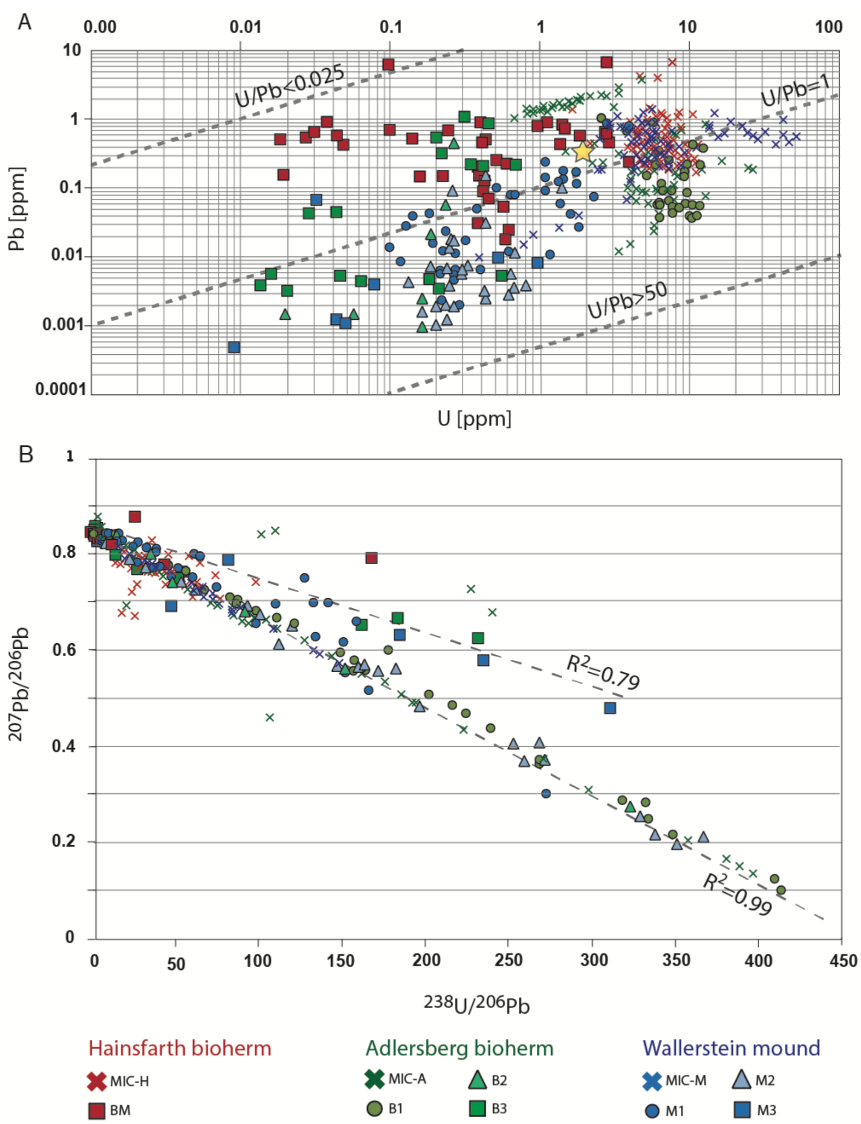

Figure 4. U and Pb geochemistry for the carbonate phases analysed from the three facies investigated. Each dot corresponds to an ablation analysis. MIC-H, MIC-A and MIC-M stand for micrite from the Hainsfarth bioherm, Adlersberg bioherm and Wallerstein mound, respectively. B1 and M1 are pendant calcite cements. B2 and M2 are isopachous calcite cements. BM, B3 and M3 are blocky calcite cements. **A)** Cross-plot of Uranium (U) *versus* Lead (Pb) concentrations expressed in parts per million (ppm). The carbonate U and Pb composition is included between the dashed lines ($0.025 < U/Pb < 50$). The yellow star represents the carbonate U and Pb mean composition after Roberts et al. (2020). **B)** Cross-plot of $^{238}U/^{206}Pb$ *versus* $^{207}Pb/^{206}Pb$ ratios and corresponding main regression line (R^2=0.99). Some data points define a different slope (R^2=0.79). In blue is the Concordia curve.

Figure 5. $^{238}U/^{206}Pb$ *versus* $^{207}Pb/^{206}Pb$ Tera-Wasserburg Concordia diagrams and corresponding absolute ages for MIC-H and BM carbonates from HAB2B6 sample (Hainsfarth bioherm, in red) and for MIC-A, B1, B2 and B3 carbonates from ME1 sample (Adlersberg bioherm, in green). Red dashed lines represent the isochrons. Blue ellipses represent the ‘n’ spot analyses and corresponding isotope ratios obtained. In blue are the Concordia curves. MIC-H, BM, MIC-A and B1 carbonate phases were analysed in different analytical sessions: ages obtained for each session are reported as vertical bars and the produced weighted average ages are indicated by asterisks. All ages are reported with 2σ confidence.

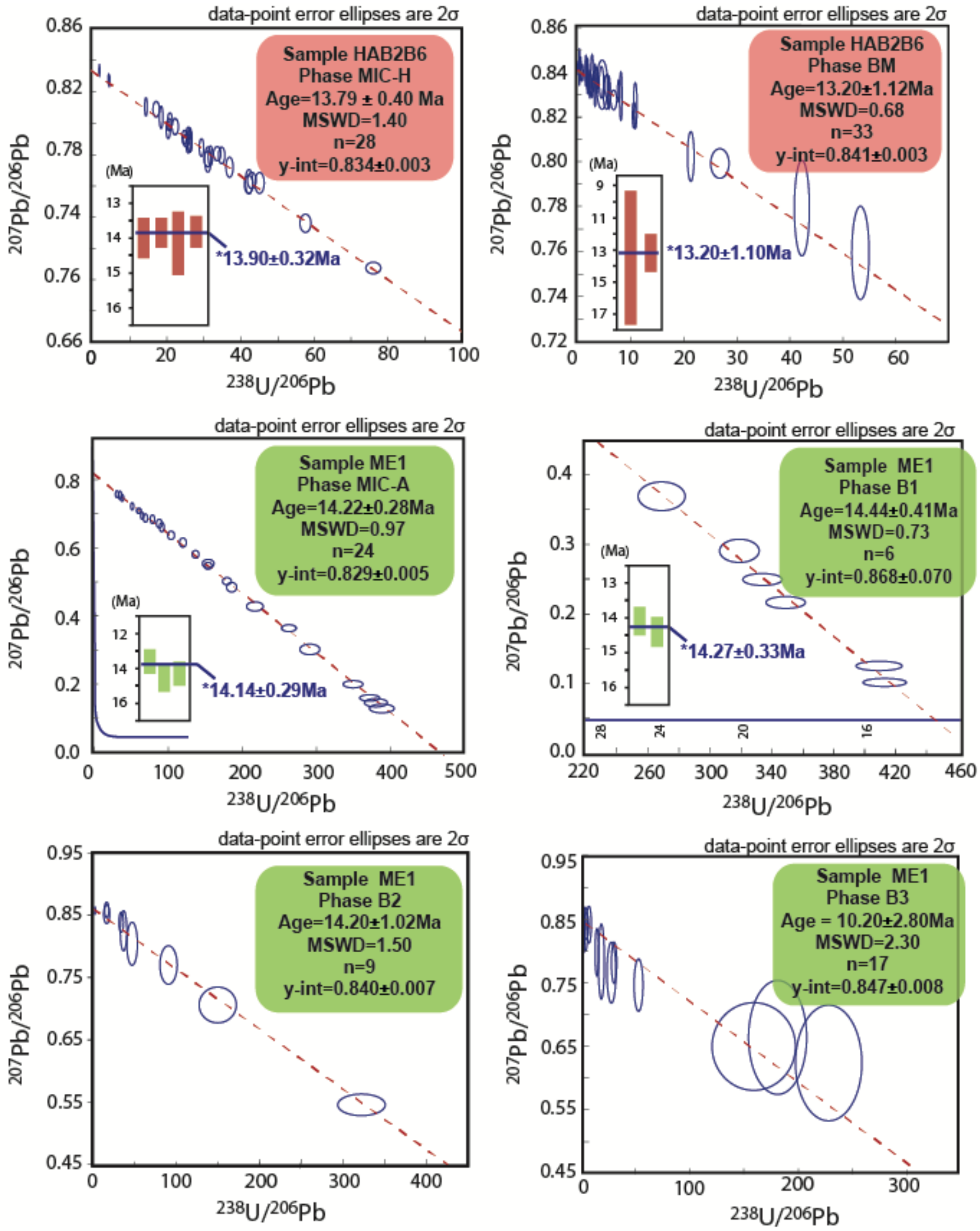
data-point error ellipses are 2σ
Sample HAB2B6
Phase MIC-H
Age=13.79 ± 0.40 Ma
MSWD=1.40
n=28
y-int=0.834±0.003
*13.90±0.32Ma
data-point error ellipses are 2σ
Sample HAB2B6
Phase BM
Age=13.20±1.12Ma
MSWD=0.68
n=33
y-int=0.841±0.003
*13.20±1.10Ma
data-point error ellipses are 2σ
Sample ME1
Phase MIC-A
Age=14.22±0.28Ma
MSWD=0.97
n=24
y-int=0.829±0.005
*14.14±0.29Ma
data-point error ellipses are 2σ
Sample ME1
Phase B1
Age=14.44±0.41Ma
MSWD=0.73
n=6
y-int=0.868±0.070
*14.27±0.33Ma
data-point error ellipses are 2σ
Sample ME1
Phase B2
Age=14.20±1.02Ma
MSWD=1.50
n=9
y-int=0.840±0.007
data-point error ellipses are 2σ
Sample ME1
Phase B3
Age = 10.20±2.80Ma
MSWD=2.30
n=17
y-int=0.847±0.008
207Pb/206Pb
238U/206Pb
(Ma)

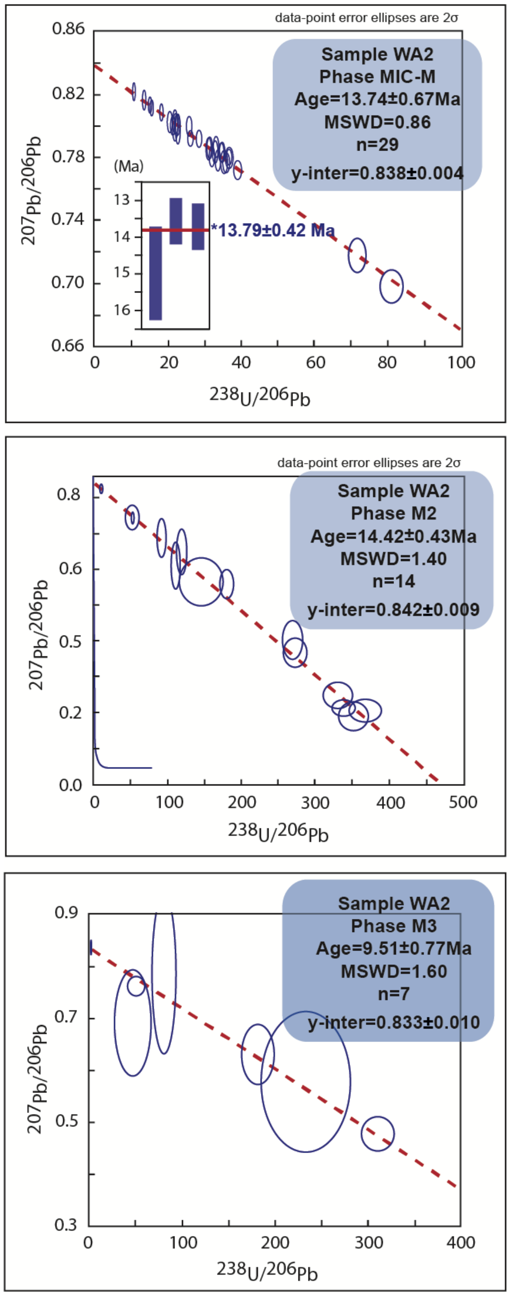

Figure 6. $^{238}U/^{206}Pb$ *versus* $^{207}Pb/^{206}Pb$ Tera-Wasserburg Concordia diagrams and corresponding absolute ages for MIC-M, M2 and M3 carbonates from WA2 sample (Wallerstein mound). Red dashed lines represent the isochrons. Ellipses represent the 'n' spot analyses and corresponding isotope ratios obtained. In blue are the Concordia curves. MIC-M phase was analysed in three analytical sessions: vertical blue bars represent the ages obtained, and the produced weighted average age is indicated by an asterisk. All ages are reported with 2σ confidence.

Facies	Sample	Phase	Age** (Ma)	2σ″	2σ$_i$^ (%)	$^{207}Pb/^{206}Pb$* ± 2σ"		n#	MSWD †	Session number	Average age• (Ma)	$\delta^{13}C$ §	$\delta^{18}O$ §	n C-O
	HAB2B6	MIC-H	13.79	0.40	2.5	0.834	0.003	28	1.40	1	13.90±0.25	0.8	0.8	2
		"	14.05	0.58	3.7	0.837	0.004	34	0.63	4				
Hainsfarth bioherm		"	13.88	0.50	3.2	0.842	0.003	43	1.07	6				
		"	14.19	0.87	5.8	0.841	0.005	31	1.30	5				
		BM	13.50	4.20	32	0.835	0.003	6	0.78	1	13.2±1.10	-5.2	-7.5	5
		"	13.20	1.12	8.3	0.841	0.003	33	0.68	6				
	ME1	MIC-A	14.22	0.28	1.3	0.829	0.005	24	0.97	2	14.14±0.20	1.9	2.6	2
		"	13.87	0.44	2.8	0.847	0.003	27	1.10	4				
		"	14.24	0.46	2.9	0.843	0.003	31	1.04	5				
Adlersberg bioherm		B1	14.15	0.35	2.0	0.854	0.006	41	1.30	3	14.27±0.33	1.5	0.3	1
		"	14.44	0.41	2.5	0.868	0.070	6	0.73	2				
		B2	14.20	1.02	7	0.840	0.007	9	1.50	2		0.7	-1.7	1
		B3	10.20	2.80	26	0.847	0.008	17	2.30	3		1.6	-6.7	3
	WA1	MIC-M	14.33	0.27	1.3	0.827	0.003	22	1.14	3		-5.0	-4.4	3
		M1	14.28	0.84	5.7	0.825	0.004	8	1.30	3		-2.8	-3.5	6
		M2	14.19	0.69	4.6	0.832	0.010	14	0.46	3		-2.9	-6.2	6
	WA2	MIC-M	13.74	0.67	4.9	0.838	0.004	29	0.85	3	13.79±0.42	-4.1	-3.3	3
Wallerstein mound		"	13.57	0.60	4.1	0.838	0.004	21	1.03	3				
		"	15.00	1.32	8.6	0.839	0.005	29	0.80	2				
		M2	14.42	0.43	2.5	0.842	0.009	14	1.40	2		-3.1	-4.1	1
		M3	9.51	0.77	8	0.833	0.010	7	1.60	2		-1.6	-8.6	2
	WA5	M1	14.70	1.81	12	0.835	0.010	28	2.10	1		-2.2	-2.5	3
	Ash15-D		2.870	0.110	3.8	0.877	0.004	24	0.99	3	2.961±0.054			
			2.980	0.110	3.7	0.872	0.003	26	1.13	1				
			2.964	0.084	2.8	0.874	0.003	24	0.94	7				
			2.972	0.068	2.3	0.874	0.004	26	0.90	4				
			3.006	0.074	2.5	0.873	0.004	26	0.61	5				
			2.919	0.050	2.4	0.863	0.016	20	0.33	8				
			2.988	0.071	2.4	0.876	0.012	26	0.57	6				

Note:

** Tera-Wasserburg diagram U-Pb lower intercept ages

" Absolute uncertainty (including long-term excess of variance of 1.5%)

^ Relative uncertaintyr: percent uncertainty of lower-intercept age (without excess of variance)

• Weighted average of n_w multiple isochron ages

* Y-axis intercept = initial Pb/Pb ratio

Number of LA-ICPMS spot analyses

† Mean Squared Weighted Deviates

§ $\delta^{13}C$ and $\delta^{18}O$ values expressed as ‰ relative to V-PDB (Vienna Pee Dee Belemnite) standard

$n^{C\text{-}O}$ number of $\delta^{13}C$ and $\delta^{18}O$ analyses

LA-session numbers and corresponding dates: 1=19/04/16; 2=20/04/16; 3=04/04/18; 4=27/02/19; 5=28/02/19; 6=17/06/19; 7=16/10/18; 8=18/06/19.

Table 3. U-Pb geochronology and C-O stable isotope data of the carbonate phases investigated. U-Pb geochronology data for the secondary standard (speleothem calcite ASH-15d) are also reported.

5. Discussion

5.1 Petrography and O-C isotope geochemistry of Ries Crater carbonates

Carbonates are common minerals that precipitate in a variety of depositional and diagenetic environments. They commonly undergo diagenetic processes such as replacement or recrystallization that may induce textural and geochemical changes (e.g. Swart, 2015). If carbonates are altered by later diagenetic processes, their U-Pb isotope system may be disturbed or even fully reset. Consequently, measured carbonate U-Pb ages may represent the timing of a later diagenetic event rather than the primary carbonate precipitation (Li et al., 2014; Mangenot et al., 2018). Therefore, petrography together with C-O stable isotope analyses were here used to: 1) define the relative timing and precipitation environments of the carbonate phases, and 2) identify the phases that potentially preserved pristine compositions.

The depositional carbonate facies investigated (Hainsfarth bioherm, Adlersberg bioherm, Wallerstein mound) consist of micrites (MIC-H, MIC-A, MIC-M) which show no petrographic evidence of major diagenetic modifications, besides minor dissolution, dolomitisation and silicification (Fig. 2, Table 2). This is in line with the preservation of low-Mg calcite ostracodes reported from the Hainsfarth bioherm facies (Christ et al., 2018). This is further supported by the covariance between micrite $\delta^{13}C$ and $\delta^{18}O$ values (R^2=0.95; Fig. 3), also reported by previous authors (e.g. Pache et al., 2001; Della Porta, 2015; Christ et al., 2018), which is typical of carbonates precipitated in closed lakes (Della Porta, 2015 and references therein). The partial dolomitisation affecting the Adlersberg bioherm micrite (MIC-A; Fig. 2C) is considered an early diagenetic process driven by lacustrine and/or meteoric phreatic fluids (e.g. Riding, 1979; Arp et al., 2017). Hence, the ages obtained for MIC-A (Table 3) should confidently reflect the timing of deposition even if ablation spots fall within both dolomitised and undolomitised portions of the micrite.

The early cementation history of the samples was driven by vadose and phreatic lacustrine fluids and is recorded by the presence of pendant (B1, M1) and isopachous (B2, M2) calcite cements (Fig. 2, Table 2). These cement types are interpreted to have precipitated together or right after the bioherm and spring mound micrites (MIC-H, MIC-A, MIC-M) that host them. They are characterized by $\delta^{13}C$-$\delta^{18}O$ covariance reasonably consistent with that defined for the depositional carbonates (micrites), though some lower $\delta^{18}O$ values also occur (Fig. 3).

The three blocky calcite cements (BM, B3 and M3) post-date the early diagenetic phases (Fig. 2). They display a distinctive CL response and negative $\delta^{18}O$ values and lack $\delta^{13}C$-$\delta^{18}O$ covariance (Fig. 2 and 3), suggesting that they resulted from different post-depositional (i.e. precipitating during later diagenesis) cementation events (e.g. Goldstein, 1991). The CL response of BM cement (Fig. 2A), together with the negative $\delta^{13}C$ and $\delta^{18}O$ values (Fig. 3), suggests precipitation from relatively early meteoric phreatic fluids. The B3 and M3 cements occur as latestpore-filling phases; their CL responses (Fig. 2D, H) and negative $\delta^{18}O$ values (Fig. 3), together with the ferroan nature of B3 (Fig. 2C), suggest precipitation from reducing fluids during burial.

The petrographic and C-O isotope analyses suggest that depositional carbonates (MIC-H, MIC-A, MIC-M micrites) and early diagenetic cements (B1, B2, M1 and M2) preserved their pristine petrographic and geochemical features. Therefore, the U-Pb ages obtained from these phases

(Table 3) may be confidently used to gather insights on the original depositional timing of these three carbonate facies. The U-Pb ages produced from the BM, B3 and M3 blocky calcite cements (Table 3) should provide information on the timing of three different post-depositional cementation events.

Figure 7. Chronostratigraphic chart of Miocene time (IUGS v 2020/01) with absolute ages for marginal and basinal facies of the Ries Crater lacustrine basin. Absolute ages for the depositional and diagenetic carbonate phases of the marginal facies (Hainsfarth bioherm, Adlersberg bioherm and Wallerstein mound) were obtained by U-Pb geochronology via LA-ICPMS. Dashed vertical bars represent weighted average ages produced by multiple LA-sessions on the same carbonate phases, as reported in Table 3. All age uncertainties (vertical bars) are reported as 2σ. Absolute ages of geomagnetic polarity chrons are from the Astronomical Tuned Neogene Time Scale (ATNTS2012). Normal and reverse polarity is indicated in black and white, respectively. The meteorite impact is considered as occurring at ~14.9Ma (after Schwarz et al., 2020 and references therein), whereas absolute ages of basinal units (A-B-C-D) are defined after Arp et al. 2013b and Rocholl et al. (2017, 2018).

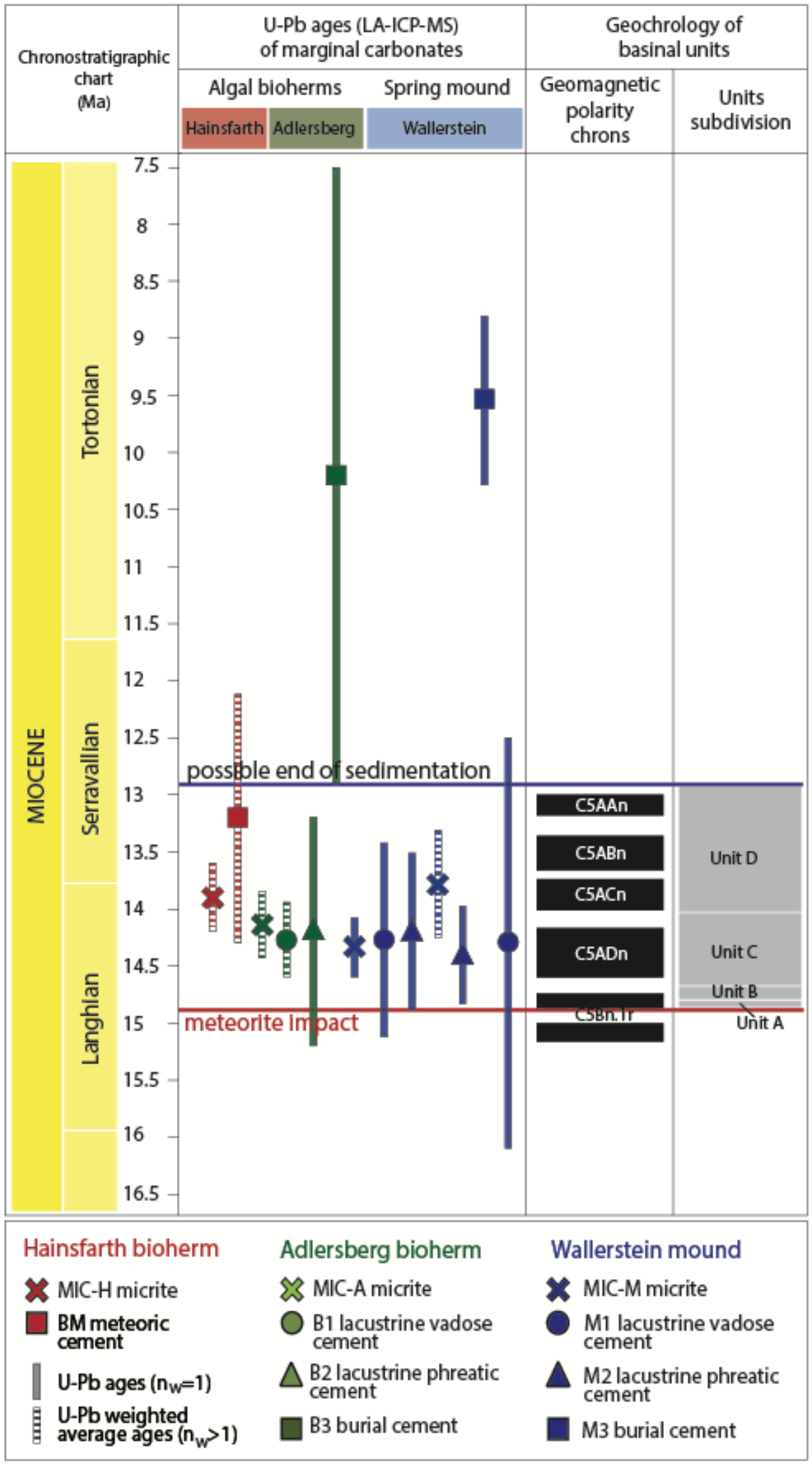
Chronostratigraphic chart (Ma)
U-Pb ages (LA-ICP-MS) of marginal carbonates
Geochrology of basinal units
Algal bioherms
Spring mound
Hainsfarth
Adlersberg
Wallerstein
Geomagnetic polarity chrons
Units subdivision
MIOCENE
Tortonian
Serravallian
Langhian
7.5
8
8.5
9
9.5
10
10.5
11
11.5
12
12.5
13
13.5
14
14.5
15
15.5
16
16.5
possible end of sedimentation
meteorite impact
C5AAn
C5ABn
C5ACn
C5ADn
C5Bn.1r
Unit D
Unit C
Unit B
Unit A
Hainsfarth bioherm
MIC-H micrite
BM meteoric cement
U-Pb ages (nw=1)
U-Pb weighted average ages (nw>1)
Adlersberg bioherm
MIC-A micrite
B1 lacustrine vadose cement
B2 lacustrine phreatic cement
B3 burial cement
Wallerstein mound
MIC-M micrite
M1 lacustrine vadose cement
M2 lacustrine phreatic cement
M3 burial cement

5.2 Ries Crater carbonate U-Pb geochronology

Multiple studies aimed to resolve the general chronostratigraphy and diagenesis of the Ries Crater lacustrine deposits and focussed on: 1) the timing of sedimentation onset and the duration of the lake life-time; 2) the margin-margin and basin-margin stratigraphic correlations; and 3) the cementation history of the marginal facies. This study reports the first U-Pb ages from both depositional and diagenetic carbonates of the Ries Crater marginal deposits. The accuracy of these ages is here discussed within the Ries Crater geological framework, well-established by previous studies (see section 2 and Data repository A).

1) Constraining the time elapsed between meteorite impact and sedimentation onset, as well as the entire lake life-time, has been attempted by several authors. The different datasets converge towards the onset of sedimentation occurring shortly after the impact (Buchner and Schmieder, 2009; Stöffler et al., 2013) and the entire succession being deposited in a time window of > 1.2 and <2 Ma (Füchtbauer et al., 1977; Pohl, 1977; Arp et al., 2017). The U-Pb ages here obtained for depositional and early diagenetic carbonate phases from marginal facies (Fig. 5 and 6, Table 3) agree with a short time gap between impact (~14.9Ma) and sedimentation onset and with the 2 Ma maximum age estimate for the lake life-time previously proposed. Further constraints on lake life-time duration may be inferred by considering the oldest and youngest U-Pb ages obtained from depositional carbonate phases (Table 3). The 14.33±0.27 Ma oldest age obtained from the micrite of the Wallerstein mound (MIC-M), which is known to be coeval with basinal unit C (Arp et al., 2013a, 2017), indicates that the marginal facies analysed presumably existed 0.57±0.27 Ma after the impact, with a lower age limit for deposition at 14.60Ma (i.e. 0.30Ma after the impact). This is in line with Arp et al. (2013b) that considered the

older basinal unit B to be deposited around 0.25Ma after the impact (see Data repository A). WA2 sample micrite (MIC-M) was not taken as the youngest sample because of disturbance of the U-Pb isotope system. Indeed, multiple dating attempts provided poorly precise ages (uncertainties up to 9%; Table 3) that are appreciably younger than the fibrous calcite cement M2 (14.42±0.43Ma) held within the same sample. Therefore, the 13.9±0.25Ma (n_w=4) age of the Hainsfarth bioherm micrite (MIC-H) was taken as the youngest of the dataset. This age suggests that sedimentation has continued at least up to 1±0.25Ma after the impact, with an upper age limit for deposition at 13.65Ma (i.e. ~1.25Ma after the impact). This is in good agreement with the >1.2Ma sedimentation duration proposed for basinal units (Füchtbauer et al., 1977; Pohl, 1977; Arp et al., 2017).

2) In the last decades, several authors attempted to establish margin-margin and basin-margin stratigraphic correlations between the Ries Crater lake deposits, based on drilling campaigns and sedimentological, geochemical and magnetostratigraphic studies (Arp et al., 2017 and references therein).

Correlations among marginal facies suggest that the Hainsfarth bioherm is younger than the Adlersberg bioherm and that the Wallerstein mound formed in a time window included between the growths of both bioherms (Arp et al., 2013a). The U-Pb ages of the three marginal facies overlap within uncertainties (Table 3, Fig. 7) and thus it is not possible to precisely assess stratigraphic correlations by taking into account the uncertainties. However, by disregarding the uncertainties, it appears that the Adlersberg bioherm ages (MIC= 14.14±0.20Ma, n_w=3; B1+B2= 14.27±0.25Ma, n_w=3, MSWD=0.59; Table 3) are older than the Hainsfarth bioherm age (MIC=13.90±0.25Ma, n_w=4; Table 3), in agreement with the correlation previously proposed by

Arp et al. (2013a). In contrast, the 14.33±0.27Ma age of micrite (MIC-M) from the Wallerstein mound, together with the weighted average age of the early diagenetic M1 and M2 cements (14.36±0.33Ma, n_w=4, MSWD=0.17; Table 3) suggest that the Wallerstein mound formed before and during the Adlersberg bioherm growth (Fig. 7), which is in conflict with what proposed by Arp et al. (2013a).

Available basin-margin stratigraphic correlations based on sedimentological and geochemical investigations suggest that the basinal C and D units are coeval with the Adlersberg and Hainsfarth bioherms, respectively (Arp et al., 2017). Age estimates for the deposition of basinal units (A-B-C-D) were here constrained by coupling the meteorite impact timing with the basinal unit magnetostratigraphy data using an approach previously presented by Arp et al. (2013b) (see section 2 and Data repository A). By combining these age estimates for basinal units with the U-Pb ages obtained in this study from marginal carbonates, it may be concluded that the three marginal facies formed during the deposition of basinal unit C and part of unit D (Fig. 7), supporting stratigraphic correlations from previous authors.

3) Different types of post-depositional cements, precipitated from fluids of meteoric to burial origin, were recognized within the Ries Crater marginal facies (Pache et al., 2001; Christ et al. 2018). Although this study mainly focuses on the timing of the marginal facies deposition, it also provides temporal constraints on the later cementations. The BM, B3 and M3 blocky calcite cements clearly display younger ages when compared to the depositional and early diagenetic phases previously discussed (Fig. 7), in line with petrography and C-O isotope geochemistry. In particular, the age of BM cement (13.20±1.10Ma, n=2; Table 3) confirms the relatively early origin from meteoric fluids. In contrast, the B3 and M3 cements reveal younger ages

respectively of 10.20±2.80Ma and 9.51±0.77Ma (Fig. 7), pointing at different burial fluid events occurring 4Ma after the deposition of the three marginal facies.

To conclude, the carbonate U-Pb ages obtained via LA-ICPMS are consistent with the petrography and C-O isotope interpretation and with the previous literature constraints on the well-established geological evolution of the Ries Crater basin. These results allow to successfully validate the geological consistency (accuracy) of the U-Pb ages obtained and confirms the potential of this dating approach to reveal the origin and time of precipitation of depositional and diagenetic carbonate phasesin other geological contexts which lack the robust independent constraints of the Ries Crater.

5.3 U-Pb carbonate chronostratigraphy in continental settings

Carbonate U-Pb geochronology is generally considered to be unsuitable for applications in stratigraphy mainly due to the large age uncertainties that are commonly obtained (Roberts et al., 2019). However, the results here presented indicate that geological contexts with poor independent time constraints, such as most continental sedimentary systems, carbonate U-Pb dating may allow successful bracketing of the depositional age of previously undateable deposits.

Future applications of carbonate U-Pb dating for chronostratigraphic purposes in continental systems will require well-established dating protocols to overcome current limitations, such as: the choice of the phases to be dated and the age accuracy and precision.

5.3.1 Protocol for sample selection

Chronostratigraphic studies require targeting of depositional (e.g. micrite, bioclasts) and/or very early diagenetic (e.g. marine, lacustrine cements) carbonate phases to yield depositional ages for continental deposits. Before dating, these phases need to be distinguished from the later ones that commonly occur in the same sample. Petrography and geochemistry studies, allowing for the reconstruction of cement stratigraphy and paragenesis (e.g. Goldstein, 1991), are necessary to establish the relative timing and precipitation environment of the different phases. This study (see sections 5.1 and 5.2) underlines their importance. Indeed, three diagenetic phases were identified prior to dating and as expected, provided younger U-Pb ages (Fig. 7).

Once the carbonate phases to be dated are identified, they need to be screened for potential diagenetic modifications using again carbonate petrography and geochemistry. Evaluating the diagenetic overprinting of depositional and early diagenetic carbonates is challenging due to the site geochemistry of the continental waters. However, it can be inferred, among others, from: 1) the crystal habitus and size (e.g. obliteration of botryoidal habitus in cements, micrite crystals > 4µm); 2) the staining and CL response (e.g. revealing ferroan nature, mottled CL); 3) the presence of micro-fracturing, crystal reaction borders and/or bi-phase fluid inclusions; 4) the $\delta^{13}C$-$\delta^{18}O$ compositions that deviate from expected values.

5.3.1 Accuracy and precision

The age precision is the key factor to understand the potentialities and limitations of the carbonate U-Pb geochronology for chronostratigraphic studies as the large uncertainties are a major limitation when dating old carbonates. Indeed, the same 1.5% age precision obtained in this study results in absolute uncertainties of 0.2-0.3Ma for Miocene carbonates and of ~8Ma for Lower Cambrian carbonates. Overall, the initial U-Th-Pb isotope composition and the dating technique chosen (e.g. ID-TIMS versus LA-ICPMS), play a crucial role in determining the final age precision. Previous authors have used carbonate U-Pb dating via bulk (i.e. ID-TIMS) and in-situ (i.e. LA-ICPMS) analyses to constrain the depositional age of lacustrine deposits of known age. These studies provide useful information to understand the limitation of these dating approaches in continental carbonate settings. Isotope dilution (ID-TIMS) U-Pb geochronology was used to date the Miocene lacustrine carbonate tufa from the Barstow Fm. (California, USA), deposited within a time window of ~5 Ma (Cole et al., 2005), which is much longer than the 2 Ma depositional time interval of the Ries Crater deposits. The ages obtained are consistent with Ar/Ar geochronology absolute constraints and are precise down to 0.9%, due to their exceptionally high U contents (up to 180 ppm). Similarly, precise U-Pb (ID-TIMS) ages were reported by Hill et al. (2016) from the Upper Cretaceous-Paleocene Colorado plateau lacustrine carbonates (U<30ppm). Geochronology by ID-TIMS is known to provide the most accurate assessment of the U-Pb age of carbonate samples. However, it is time consuming and labour intensive and it may have a lower success rate due to the limited spatial-resolution (Roberts et al., 2020), particularly because high and low $^{238}U/^{206}Pb$ domains are heterogeneously distributed at the sub-mm scale in carbonates (Rasbury and Cole, 2009).

In situ (LA-ICPMS) U-Pb geochronology was used by Frisch et al. (2019) to date the Miocene alluvial-lacustrine carbonates (U<10 ppm) from the Aktau succession (Kazakhstan). The ages reported show a very good correlation with magnetostratigraphy and cyclostratigraphy data and are precise down to 3% (2σ). New advances on 2D elemental and isotopic ratio mapping allowed Drost et al. (2018) to produce ages with uncertainties down to 1% from early diagenetic carbonate cements (U<40ppm) of the Carboniferous-Permian Rothenburg Fm. (Germany). The results are consistent with biostratigraphic constraints and zircon U-Pb geochronology from interbedded ash layers and encourage the application of this dating approach also in Paleozoic continental carbonate systems.

The U-Pb (LA-ICPMS) technique was chosen in this study because it has many key benefits compared to the bulk techniques: the dating procedure is simpler, faster and analyses are preformed directly on thin sections with sampling (ablation) spot sizes of <0.2mm. This allows discarding diagenetically altered areas and enables dating volumetrically minor carbonate phases. Moreover, non-systematic (random) sample pre-screening can be performed prior to analysis to identify areas with high and variable $^{238}U/^{206}Pb$. These technical advantages significantly enhance the success rate of carbonate U-Pb dating even if LA-ICPMS is considered to be analytically less precise than ID-TIMS (Roberts et al., 2020). In the present study, various carbonates phases with U concentrations below 10ppm provided accurate depositional ages with precision mostly included between 1.5 and 3% (2σ), after propagating all necessary uncertainties. Repeated measurements on the same carbonate phases yielded consistent ages within analytical uncertainties, allowing assessment of the long-term reproducibility of the method (Table 3, Data repository G.1). Depositional and early diagenetic carbonates yielded consistent ages (Fig. 7) since the weighted average age of depositional carbonates (MIC-H, MIC-A, MIC-M) of 14.09±0.18Ma (MSWD=1.5; n_w=11) is within uncertainty indistinguishable from the 14.30±0.20Ma (MSWD = 0.3; n_w = 7) weighted average age of the early diagenetic carbonates (B1, M1, B2, M2). This suggests that both carbonate types may potentially be used as reliable geochronometers, as long as they retain their pristine geochemical compositions. The depositional carbonates (micrites) seem to have a higher dating potential since they provided more precise ages (internal uncertainties between 1.3 to 4.7%, in 9 out of 11 samples) if compared to the early diagenetic cements. This is most likely due to the interplay of three factors characterizing the micrite samples: 1) higher U/Pb variability, 2) higher U (> 2ppm) concentrations, combined with 3) relatively lower initial Pb (Fig. 4). In contrast, the early diagenetic cements (B1, M1, B2 and M2), precipitated from lacustrine fluids, display about 30% less precise ages (internal uncertainties between 1.9 to 7%, in 6 out of 7 samples).

Overall, this study indicates that U-Pb carbonate geochronology may confidently assist stratigraphic studies at the time resolution of 3rd order depositional sequences (0.5-5Ma) and encourage the use of U-Pb (LA-ICPMS) technique as a chronostratigraphic tool for carbonates from lacustrine (and more broadly continental) settings, where other commonly applied chrono-chemo-bio-stratigraphic approaches may be insufficient and chronostratigraphic correlations are usually out of reach.

Conclusions

Depositional carbonates (micrites), together with early diagenetic (lacustrine) and post-depositional (meteoric and burial) calcite cements from marginal facies of the Ries Crater impact basin were investigated. Petrography and C-O stable isotope analyses indicate that depositional and early diagenetic carbonate phases preserved pristine geochemical composition and therefore are ideal targets to apply *in-situ* U-Pb geochronology (LA-ICPMS) in order to constrain the facies depositional timing, whereas later diagenetic phases may inform on the post-depositional cementation history.

All carbonates were successfully dated. U-Pb ages of micrites and early diagenetic cements (between 14.7±1.81 and 13.9±0.25Ma) are consistent with the geological and geochronological constraints offered by the well constrained Ries Crater basin, validating the accuracy of the dataset and of the applied method. In particular, the U-Pb dataset indicates a very short time elapsed between meteorite impact and sedimentation onset and matches the independent estimates of the minimum and maximum duration of lake life-time. The consistency between depositional and early diagenetic carbonate ages underlines that both carbonate types may suitably be used for U-Pb geochronology. Finally, three later calcite cements were also dated at 13.20±1.1Ma, 10.20±2.80Ma and 9.51±0.77Ma, indicating that the basin was punctuated by different post-depositional cementation events.

Overall, the time-resolution achieved by the U-Pb (LA-ICPMS) technique for Miocene carbonates (down to 1.5%, 2σ; about 0.2-0.3Ma) was adequate to bracket the depositional age of the marginal facies investigated and to correlate them with siliciclastic basinal units in a time window <2Ma. This study conclusively suggests that, with suitable protocol for sample selection, it is possible to obtain geologically consistent and precise ages from depositional and diagenetic continental carbonates that may confidently assist chronostratigraphic studies at the resolution of the 3rd order depositional sequences (0.5-5Ma).

ACKNOWLEDGMENTS

We are grateful to E. Bemer (IFP Energies nouvelles) for funding the survey in the framework of D. Montano's Master project at the University of Milan. Manuscript writing was undertaken in the framework of D. Montano's PhD project funded by IFP Energies nouvelles. S. Rohais (IFP Energies nouvelles) is acknowledged for his guidance and scientific support during the PhD project. Prof. M. Joachimski (GeoZentrum Nordbayern) is thanked for O-C stable isotope analysis of carbonates. The Fürst Wallerstein Braurei is thanked for allowing publication of analytical data on three Wallerstein mound samples collected in their property. The manuscript benefitted of significant improvements from the careful revisions of Prof. David Chew and an anonymous reviewer. This is FIERCE contribution No. XX.

References

Arp, G., 1995. Lacustrine bioherms, spring mounds, and marginal carbonates of the Ries-impact-crater (Miocene, Southern Germany). Facies. 33 (1), 35-89. https://doi.org/10.1007/bf02537444.

Arp, G., Blumenberg, M., Hansen, B.T., Jung, D., Kolepka, C., Lenz, O., Nolte, N., Poschlod, K., Reimer, A., Thiel, V., 2013a. Chemical and ecological evolution of the Miocene Ries impact crater lake, Germany: a re-interpretation based on the Enkingen (SUBO 18) drill core. Geol Soc Am Bull. 125 (7-8), 1125-1145. https://doi.org/10.1130/B30731.1.

Arp G., Hansen B. T., Pack A., Reimer A., Schmidt B. C., Simon K., and Jung D., 2017. The soda lake—mesosaline halite lake transition in the Ries impact crater basin (drilling Löpsingen 2012, Miocene, southern Germany). Facies. 63 (1). https://doi.org/10.1007/s10347-016-0483-7.

Arp, G., Kolepka, C., Simon, K., Karius, V., Nolte, N., Hansen, B. T., 2013b. New evidence for persistent impact-generated hydrothermal activity in the Miocene Ries impact structure, Germany. Meteorit. Planet Sci. 45 (12), 2491–2516 https://doi.org/10.1111/maps.12235.

Arp, G., Reimer, A., Simon, K., Sturm, S., Wilk, J., Kruppa, C., Hecht, L., Hansen, B.T., Pohl, J., Reimold, W.U., Kenkmann, T., Jung, D. 2019. The Erbisberg drilling 2011: Implications for the structure and postimpact evolution of the inner ring of the Ries impact crater. Meteorit. Planet. Sci. 1-35. https://doi.org/10.1111/maps.13293.

Bohacs, K. M., Carroll, A. R., Neal, J. E., Mankiewicz P. J., 2000. Lake-basin type, source potential, and hydrocarbon character: an integrated-sequence-stratigraphic–geochemical framework, in: E. H. Gierlowski-Kordesch & K. R. Kelts, eds., Lake basins through space and time: AAPG Studies in Geology. 46, 3–34. https://doi.org/10.1306/St46706C1.

Bolten R., and Müller D., 1969. Das Tertiär im Nördlinger Ries und in seiner Umgebung. Geol. Bavarica. 61, 87-130.

Buchner, E., Schwarz, W. H., Schmieder, M., Trieloff, M., 2010. Establishing a 14.6 ± 0.2 Ma age for the Nördlinger Ries impact (Germany)—A prime example for concordant isotopic ages from various dating materials. Meteorit. Planet. Sci. 45 (4). https://doi.org/10.1111/j.1945-5100.2010.01046.x.

Buchner, E. and Schmieder, M. 2009. Multiple fluvial reworking of impact ejecta-A case from the Ries crater, southern Germany. Meteoritics & Planetary Science 44, Nr 7, 1051-1060. https://doi.org/10.1111/j.1945-5100.2009.tb00787.x.

Christ, N., Maerz, S., Kutschera, E., Kwiecien, O., Mutti, M., 2018. Palaeoenvironmental and diagenetic reconstruction of a closed-lacustrine carbonate system – the challenging marginal setting of the Miocene Ries Crater Lake (Germany). Sedimentology. 65 (1). https://doi.org/ 10.1111/sed.12401.

Cole, J. M., Rasbury, E. T., Hanson, G. N., Montañez, I. P., Pedone, V. A., 2005. Using U-Pb ages of Miocene tufa for correlation in a terrestrial succession, Barstow Formation, California. Geol. Soc. Am. Bull. 223 (3), 127-146. https://doi.org/10.1130/B25553.1.

Della Porta, G. 2015. Carbonate build-ups in lacustrine, hydrothermal and fluvial settings: comparing depositional geometry, fabric types and geochemical signature In: Bosence, D. W. J., Gibbons, K. A., Le Heron, D. P., Morgan, W. A., Pritchard, T. & Vining, B. A. (eds), Microbial Carbonates in Space and Time: Implications for Global Exploration and Production. Geological Society, London, Special Publications, 418, 17-68. http://dx.doi.org/10.1144/SP418.4

Deschamps, R., Rohais, S., Hamon, Y., Gasparrini, M. 2020. Dynamic of a lacustrine sedimentary system during late rifting at the Cretaceous–Palaeocene transition: Example of the Yacoraite Formation, Salta Basin, Argentina. Depositional Rec. 00:1-34. https://doi.org/10.1002/dep2.116.

Dickson, J. A. D., 1966. Carbonate identification and genesis as revealed by staining. J. Sediment. Res. 36 (2), 491–505. https://doi.org/10.1306/74D714F6-2B21-11D7-8648000102C1865D.

Drost, K., Chew, D., Petrus, J. A., Scholze, F., Woodhead, J. D., Schneider, J. W., & Harper, D. A. T. 2018. An image mapping approach to U-Pb LA-ICP-MS carbonate dating and applications to direct dating of carbonate sedimentation. Geochemistry, Geophysics, Geosystems, 19, 4631–4648. https://doi.org/10.1029/2018GC007850.

Frisch, K., Voigt, S., Verestek, V., Appel, E., Albert, R., Gerdes, A., Arndt, I., Raddatz, J., Voigt, T., Weber, Y., Batenburg, S.J. 2019. Laser ablation Uranium-Lead dating of the Miocene alluvial-lacustrine Aktau succession in south-east Kazakhstan. PANGAEA. https://doi.org/10.1594/PANGAEA.906093.

Füchtbauer, H., von der Brelie, G., Dehm, R., Förstner, U., Gall, H., Höfling, R., Hoefs, J., Hollerbach, A., Hufnagel, H., Jankowski, B., Jung, W., Malz, H., Mertes, H., Rothe, P., Salger, M., Wehner, H., Wolf, M., 1977. Tertiary lake sediments of the Ries, research borehole Nördlingen 1973—A summary. 75, 13-19. Geol. bavarica.

Gerdes, A. and Zeh, A., 2009. Zircon formation versus zircon alteration-new insights from combined V-Ph and Lu-Hf in situ LA-ICP-MS analyses, and consequences for the interpretation of Archean zircon from the Central Zone of the Limpopo Belt. Chem. Geol. 261 (3-4), 230-243. https://doi.org/ 10.1016/j.chemgeo.2008.03.005.

Godeau, N., Deschamps, P., Guihou, A., Leonide, P., Tendil, A., Gerdes, A., Hamelin, J.G., 2018. U-Pb dating of calcite cement and diagenetic history in microporous carbonate reservoirs: case of the Urgonian Limestone, France. Geology. 46 (3), 247-250. https://doi.org/10.1130/G39905.1.

Guillong, M., Wotzlaw, J. F., Looser, N., and Laurent, O. 2020. Evaluating the reliability of U–Pb laser ablation inductively coupled plasma mass spectrometry (LA-ICP-MS) carbonate geochronology: matrix issues and a potential calcite validation reference material. Geochronology. 2, 155–167, https://doi.org/10.5194/gchron-2-155-2020.

Hansman, R. J., Albert, R., Gerdes, A., Ring, U., 2018. Absolute ages of multiple generations of brittle structures by U-Pb dating of calcite. Geology. 46 (3), 207-210. https://doi.org/10.1130/G39822.1.

Hill, C. A., Polyak, V. J., Asmerom, Y., Provencio, P. P. 2016. Constraints on a Late Cretaceous uplift, denudation, and incision of the Grand Canyon region, southwestern Colorado Plateau, USA, from U-Pb dating of lacustrine limestone. 35 (4), 896-906. https://doi.org/10.1002/2016TC004166.

Jankowski B., 1977. Die Postimpakt-Sedimente in der Forschungsbohrung Nördlingen 1973. *Geol. Bavarica.* 75, 21– 36.

Jankowski, B. 1981. Die Geschichte der Sedimentation im Nördlinger Ries und Randecker Maar. Bochumer geologische und geotechnische Arbeiten 6: 1– 315.

Li, Q., Parrish, R. R., Horstwood, M. S. A., McArthur, J. M. 2014. U–Pb dating of cements in Mesozoic ammonites. Chem. Geo. 376, 7683. http://dx.doi.org/10.1016/j.chemgeo.2014.03.020.

Ludwig, K. R. 2012. User's Manual for Isoplot Version 3.75–4.15: a Geochronological Toolkit for Microsoft Excel Berkeley Geochronological Center Special Publication, 5 (2012)

Mangenot, X., Gasparrini, M., Gerdes, A., Bonifacie M., Rouchon V. 2018. An emerging thermochronometer for carbonate-bearing rocks: Δ_{47}/(U-Pb). Geology. 46 (12), 1067-1070. https://doi.org/10.1130/G45196.1.

MacDonald, J. M., Faithfull, J. W., Roberts, N. M. W., Davies, A. J., Holdsworth, C. M., Newton, M., Williamson, S., Boyce, A., John, C. M. 2019. Clumped-isotope palaeothermometry and LA-ICP-MS U–Pb dating of lava-pile hydrothermal calcite veins. Contrib Mineral Petrol, 174, 63. https://doi.org/10.1007/s00410-019-1599-x.

Mason, A. J., Henderson, G. M., Vaks, A. 2016. An Acetic Acid-Based Extraction Protocol for the Recovery of U, Th and Pb from Calcium Carbonates for U-(Th)-Pb Geochronology. Geostand. Geoanalytical Res, 37 (3), 261-275. https://doi.org/10.1111/j.1751-908X.2013.00219.x.

Nuriel, P., Craddock, J., Kylander-Clark, A. R., Uysal, T., Karabacak, V., Dirik, R. K., Hacker, B. R. and Weinberger, R. 2019. Reactivation history of the North Anatolian fault zone based on calcite age-strain analyses. Geology, 47, 465-469. https:// doi.org/10.1130/G45727.1.

Nuriel, P., Wotzlaw, J., Ovtcharova, M., Vaks, A., Stremtan, C., Šala, M., Roberts, N. M. W., Kylander-Clark, A. R. C., 2020, in review. The use of ASH-15 flowstone as a matrix-matched reference material for laser-ablation U-Pb geochronology of calcite. Geochronology Discuss. https://doi.org/10.5194/gchron-2020-22.

Pache, M., Reitner, J., Arp, G., 2001. Geochemical evidence for the formation of a large Miocene “travertine” mound at a sublacustrine spring in a soda lake (Wallerstein Castle Rock, Nördlinger Ries, Germany). Facies. 45 (1), 211-230. https://doi.org/10.1007/BF02668114.

Pohl, V. J. 1977. Paläomagnetische und gesteinsmagnetische Untersuchungen an den Kernen der Forschungsbohrung Nördlingen 1973. Geologica Bavarica 75, 328-348.

Pohl, J., Poschlod, K., Reimold, W. U., Meyer, C., Jacob, J., 2010. Ries crater, Germany: The Enkingen magnetic anomaly and associated drill core SUBO 18. In: Roger, L., Gibson, L., Reimold,

W. U. (Eds.), Large Meteorite Impacts and Planetary Evolution IV, https://doi.org/10.1130/2010.2465(10).

Rasbury, E. T. and Cole, J. M., 2009. Directly dating geologic events: U-Pb dating of carbonates. Rev. Geophys. 47 (3). https://doi.org/10.1029/2007RG000246.

Riding, R., 1979. Origin and diagenesis of lacustrine algal bioherms at the margin of the Ries crater, Upper Miocene, southern Germany. Sedimentology. 26 (5), 645-680. https://doi.org/10.1111/j.1365-3091.1979.tb00936.x.

Roberts, N., Drost, K., Horstwood, M., Condon, D. J., Chew, D., Drake, H., Milodowski, A. E., McLean, N. M., Smye, A., Walker, R. J., Haslam, R., Hodson, K., Imber, J. Beaudoin, N. 2020. LA-ICP-MS U-Pb carbonate geochronology: strategies, progress, and application to fracture-fill calcite. Geochronology Discussion, Copernicus Gesellschaft mbH. https://doi.org/ 10.5194/gchron-2019-15. In press, 2020.

Roberts, N. M. W., Rasbury, T., Parrish, R. R., Smith, C. J. M., Horstwood, M. S. A., Condon, B. J., 2017. A calcite reference material for LA-ICP-MS U-Pb geochronology. Geochem. Geophys. 18 (7), 2807-2814. https://doi.org/ 10.1002/2016GC006784.

Rocholl, A., Böhme, M., Gilg, H. A., Pohl J., Schaltegger, U., Wijbrans, J. 2018. Comment on ‘‘A high-precision $^{40}Ar/^{39}Ar$ age for the Nördlinger Ries impact crater, Germany, and implications for the accurate dating of terrestrial impact events” by Schmieder et al. (Geochim. et Cosmochim. Acta 220 (2018) 146–157). Geochim. et Cosmochim. Acta. 238, 599–601. https://doi.org/10.1016/j.gca.2018.05.018.

Rocholl, A., Schaltegger, U., Gilg, H. A., Wijbrans, J., Böhme, M., 2017. The age of volcanic tuffs from the Upper Freshwater Molasse (North Alpine Foreland Basin) and their possible use for tephrostratigraphic correlations across Europe for the Middle Miocene. Int. J. Earth Sci. 107 (2), 387-407. https://doi.org/10.1007/s00531-017-1499-0.

Rohais, S., Hamon, Y., Deschamps, R., Beaumont, V., Gasparrini, M., Pillot, D., Romero-Sarmiento, M. F. 2019. Patterns of organic carbon enrichment in a lacustrine system across the K-T boundary: Insight from a multi-proxy analysis of the Yacoraite Formation, Salta rift basin, Argentina. International Journal of Coal Geology. 210. https://doi.org/10.1016/j.coal.2019.05.015.

Scardia, G., Parenti, F., Miggins, D. P., Gerdes, A., Araujo, A. G., and Neves, W. A. 2019. Chronologic constraints on hominin dispersal outside Africa since 2.48 Ma from the Zarqa Valley, Jordan, Quaternary Sci. Rev., 219, 1–19. https://doi.org/10.1016/j.quascirev.2019.06.007.

Schmieder, M., Kennedy, T., Jourdan, F., Buchner, E., Reimold, W.U., 2018a. A high-precision $^{40}Ar/^{39}Ar$ age for the Nördlinger Ries impact crater, Germany, and implications for the accurate dating of terrestrial impact events. Geochim. Cosmochim. Acta. 220, 46-157. https://doi.org/10.1016/j.gca.2017.09.036.

Schmieder, M., Kennedy, T., Jourdan, F., Buchner, E., Reimold, W. U., 2018b. Comment on “A high-precision $^{40}Ar/^{39}Ar$ age for the Nördlinger Ries impact crater, Germany, and implications for the accurate dating of terrestrial impact events.” By Schmieder et al. (Geochim. Cosmochim. Acta. 2018). 238, 599-601. https://doi.org/10.1016/j.gca.2018.05.018.

Schwarz, H. W., Hanel, M., Trieloffet, M. 2020. U-Pb dating of zircons from an impact melt of the Nördlinger Ries crater. Meteoritics & Planetary Science 55, Nr 2, 312–325. https://doi.org/ 10.1111/maps.13437.

Shoemaker, M. C., and Chao, E. 1961. New evidence for the impact origin of the Ries basin, Bavaria, Germany. J. Geophys. Res. 66 (10), 3371-3378. https://doi.org/10.1029/JZ066i010p03371.

Stacey, J. S., Kramers, J. D. 1975. Approximation of terrestrial lead isotope evolution by a two-stage model. EPSL. 26 (2), 207-221. https://doi.org/10.1016/0012-821X(75)90088-6.

Stöffler, D., Artemieva, N. A., Wünnemann K., Reimold, W. U., Jacob, J., Hansen B. K., Summerson, I. A. T., 2013. Ries crater and suevite revisited—Observations and modeling Part II: Modeling. *Meteorit. Planet. Sci.* 48 (4), 590-627. https://doi.org/10.1111/maps.12086.

Swart, P. K., 2015. The geochemistry of carbonate diagenesis: The past, present and future. *Sedimentology*, 62, 1233-1304. https://doi.org/10.1111/sed.12205.

Veizer, J., Ala, D., Azmy, K., Bruckschen, P., Buhl, D., Bruhn, F., Carden, G.A., Diener, A., Ebneth, S., Godderis, Y. and Jasper, T., 1999. $^{87}Sr/^{86}Sr$, $\delta^{13}C$ and $\delta^{18}O$ evolution of Phanerozoic seawater. Chemical geology. 161 (13), 59-88.

Kurumada, Y., Aoki, S., Aoki, K., Kato, D., Saneyoshi, M., Tsogtbaatar, K., Windley, B. F., Ishigaki, S. 2020. Calcite U–Pb age of the Cretaceous vertebrate-bearing Bayn Shire Formation in the Eastern Gobi Desert of Mongolia: Usefulness of caliche for age determination. Terra Nova, 00:1-7. https://doi.org/10.1111/ter.12456.

Data repository

Data repository A. In the last decade the Ries Crater meteorite impact was dated by several authors (e.g., Buchner et al., 2010; Rocholl et al., 2017, 2018; Schmieder et al., 2018a,b; Schwarz et al., 2020), with ages ranging between 15.00±0.03Ma (zircons U-Pb dating; Rocholl et al., 2018) and 14.50±0.32Ma (Ar-Ar dating of recrystallized feldspars; Buchner et al., 2010). The 0.5Ma disagreement between these ages can be related to multiple factors as discussed by Rocholl et al. (2018), Schmieder et al. (2018a, b) and Schwarz et al. (2020). In this contribution we consider the impact as occurring at around 14.9 Ma, in line with most of the absolute ages published in the last decade (Schwarz et al., 2020 and references therein).

Absolute age estimates for the deposition of basinal units (A-B-C-D; Füchtbauer et al., 1977; Jankowski, 1977) was achieved by coupling the meteorite impact timing with the basinal unit magnetostratigraphy, as previously done by Arp et al. (2013). Accordingly, the impact related suevite (i.e. melt bearing crystalline breccia; Stöffler et al., 2013) records a distinctive reverse magnetization and at the top the transition to normal polarity (Pohl, 1977; Pohl et al., 2010; Fig. A.1). As a consequence, the impact is supposed to occur at the top of a reverse magnetization stage.

Based on the absolute ages of geomagnetic polarity chrons by Hilgen et al. (2012) the meteorite impact was possibly allocated at the top of C5Bn.1r (15.03 to 14.87 Ma) or C5ADr (14.77 to 14.61 Ma) reverse chrons (Buchner et al., 2013; Rocholl et al., 2017; Schmieder et al., 2018a,b). The ~14.9Ma impact timing would therefore correspond to the top of C5Bn.1r (14.87Ma), in agreement with the interpretation of Rocholl et al. (2017, 2018).

The Ries Crater sedimentation onset is known to have occurred shortly after the impact (Buchner and Schmieder, 2009; Stöffler et al., 2013) as demonstrated by the weathering of the impactites driven by meteoric fluids (Muttik et al., 2011) and the short-distance fluvial transport of impact related breccia (Arp et al., 2019). However, the exact time elapsed between the impact and the onset of sedimentation is at today unconstrained (Schmieder et al., 2018b).

Pohl (1977) suggest that unit A sediments were deposited in a few thousand years at the most and Arp et al. (2013) indicated that basinal unit B was deposited around 0.25Ma after the impact, which also implies a very short time gap between meteorite impact and sedimentation onset.Indeed, in 0.25Ma both unit A and part of unit B (at least 150m of sediments) were already accumulated in the basin. Consequently, it can be deduced that the first basinal sediments (unit A) were deposited during the C5Bn.1n chron that follows C5Bn.1r (Fig. A1).

In conclusion, the absolute age estimate for the four basinal units was constrained as follows: unit A is here considered to be deposited during C5Bn.1n; the transition from unit B to unit C is inside C5Adr chron and the onset of unit D deposition was allocated at ~14 Ma, at the limit between C5ACr and C5ACn chrons. This latter estimate is due to Pohl (1977) who highlights a transition from reverse to normal polarity at the base of unit D.

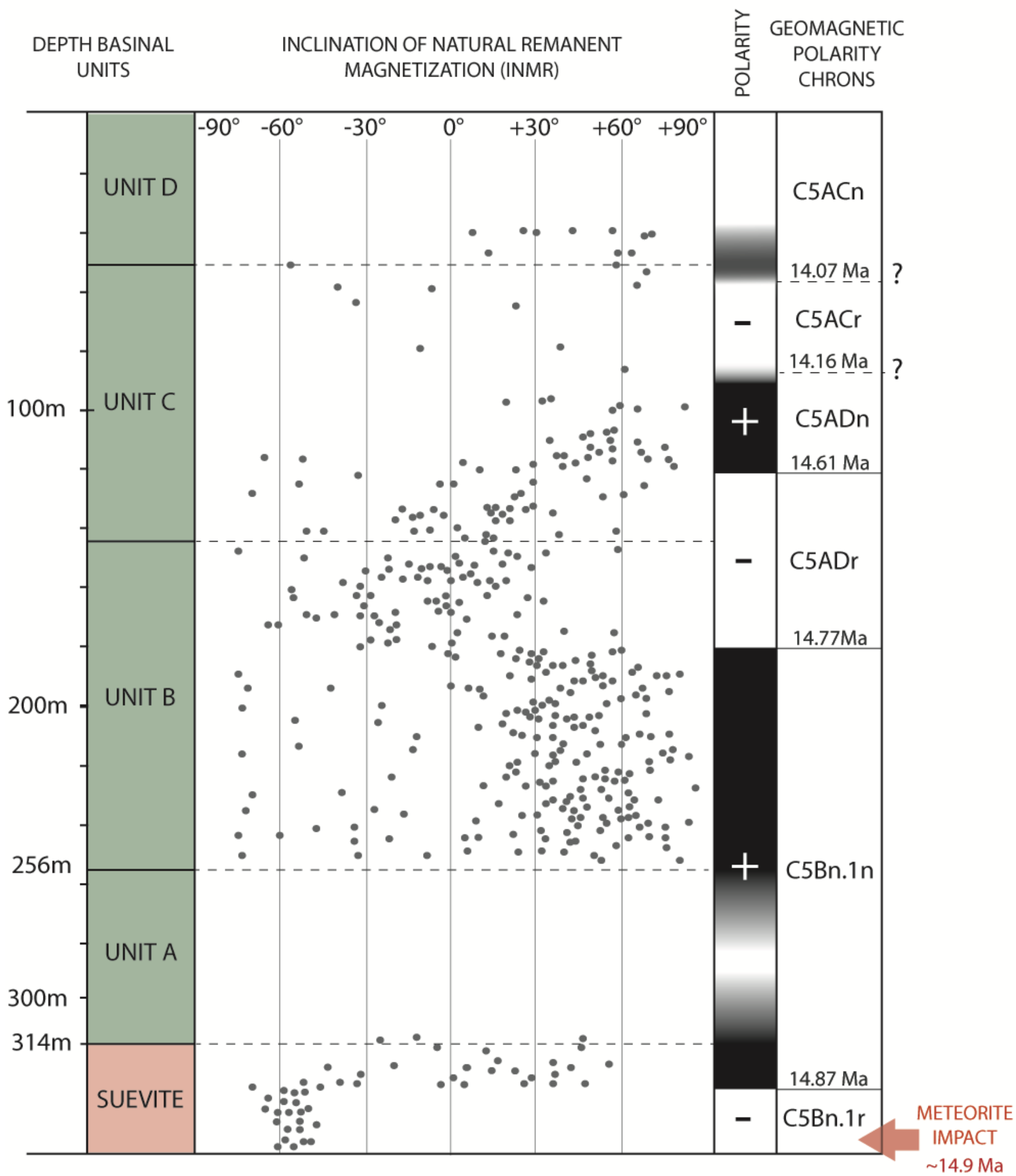

Figure A.1

Chart summarizing data from the Nördlingen 1973 borehole. Basinal lithostratigraphic units according to Füchtbauer et al. (1977) and Jankowski (1977) with corresponding Inclination of Natural Remnant Magnetization (INRM) and polarity from Pohl (1977) and Pohl et al. (2010).

Normal and reverse polarity are indicated in black and white, respectively, whereas grey areas indicate insufficient INRM data and uncertain polarity. Absolute ages of geomagnetic polarity chrons are from the Astronomical Tuned Neogene Time Scale (ATNTS2012) of Hilgen et al. (2012).

Data repository B

Table B.1 $\delta^{13}C$ and $\delta^{18}O$ values for the ten carbonate phases analysed are reported in ‰ relative to the Vienna-Pee Dee Belemnite (V-PDB) standard. Most of the carbonate phases were analysed more than once in order to account for possible heterogeneities of their C-O stable isotope composition. BL isopachous fibrous cement from the Hainsfarth bioherm and DOL from the Adlersberg bioherm (described in Figure 2 and in Table 2) could not be micro-sampled and were therefore not analysed.

Facies	Sample	Phase	$\delta^{13}C$ (‰V-PDB)	$\delta^{18}O$, (‰V-PDB)
Hainsfarth bioherm	HAB2B6	MIC-H	1.47	2.51
			0.12	-0.93
		Bm	-5.30	-7.76
			-5.34	-7.48
			-5.09	-7.46
			-5.45	-7.37
			-4.98	-7.28
Adlersberg bioherm	ME1	MIC-A	1.25	1.91
			2.50	3.31
		B1	1.54	0.26
		B2	0.70	-1.73
		B3	1.41	-7.54
			1.50	-6.71
			1.95	-5.97
Wallerstein mound	WA1	MIC-W	-4.92	-4.15
			-5.53	-5.11
			-4.43	-4.04
		M2	-2.64	-3.01
			-2.99	-3.75
			-2.12	-5.04
			-3.21	-1.88
			-3.00	-3.87
			-2.64	-3.46
		M3	-2.42	-5.92
			-2.59	-6.08
			-3.42	-5.74
			-2.71	-6.86
			-3.30	-6.30
			-2.83	-6.51
	WA2	MIC-W	-4.21	-3.44
			-4.88	-4.02
			-3.09	-2.58
		M2	-3.06	-4.12
		M3	-1.58	-9.60
			-1.57	-7.58
	WA5	MIC-W	-2.93	-3.58
		M1	-2.48	-0.79
			-1.98	-2.33
			-2.25	-4.24
		M3	-2.96	-6.19
			-2.24	-6.93

Data repository C

Table C.1

U-Pb carbonate geochronology LA-ICPMS raw data. The dataset is corrected offline using a macro-based in-house MS Excel© spreadsheet.

Data repository D

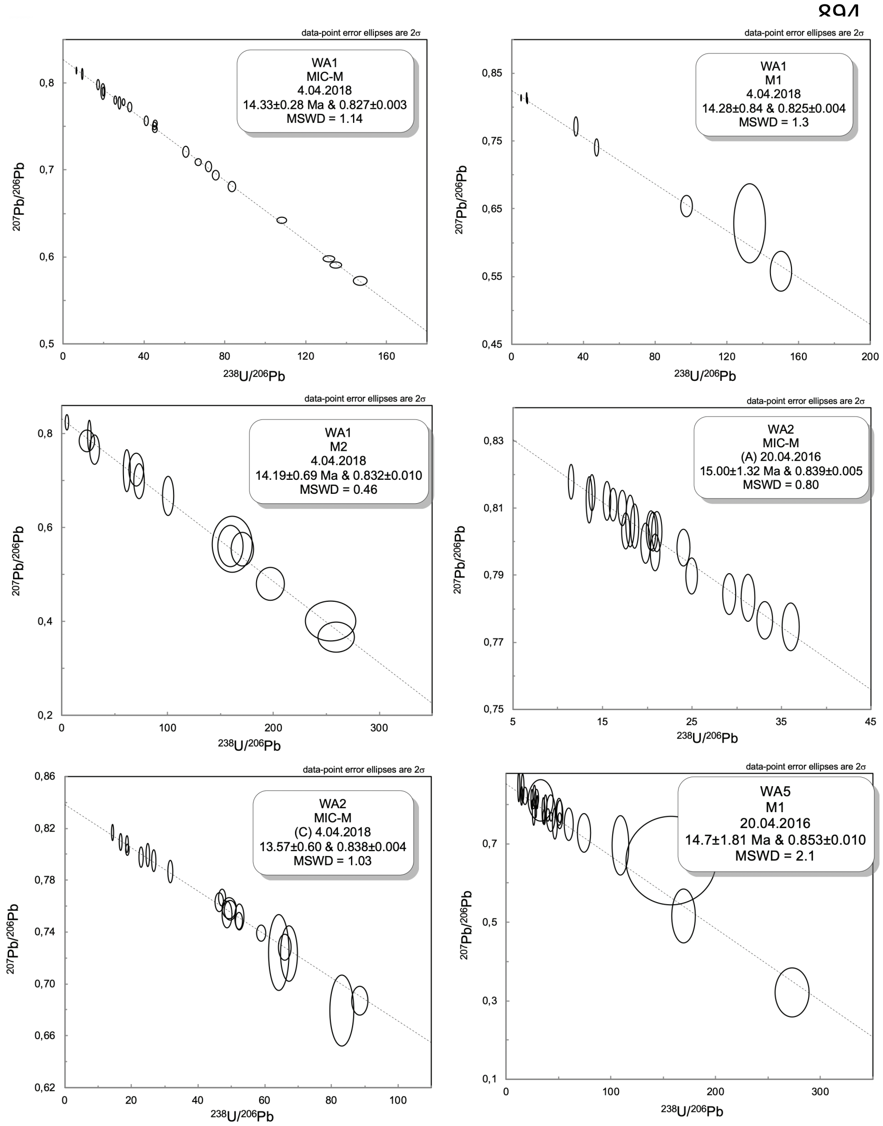

Figure D.1 $^{238}U/^{206}Pb$ *versus* $^{207}Pb/^{206}Pb$ Tera-Wasserburg Concordia diagrams and corresponding absolute ages for the Wallerstein mound samples (WA1, WA2 and WA5). Dashed lines represent the isochrons. Ellipses represent the 'n' spot analyses and corresponding isotope ratios obtained.

Data repository E

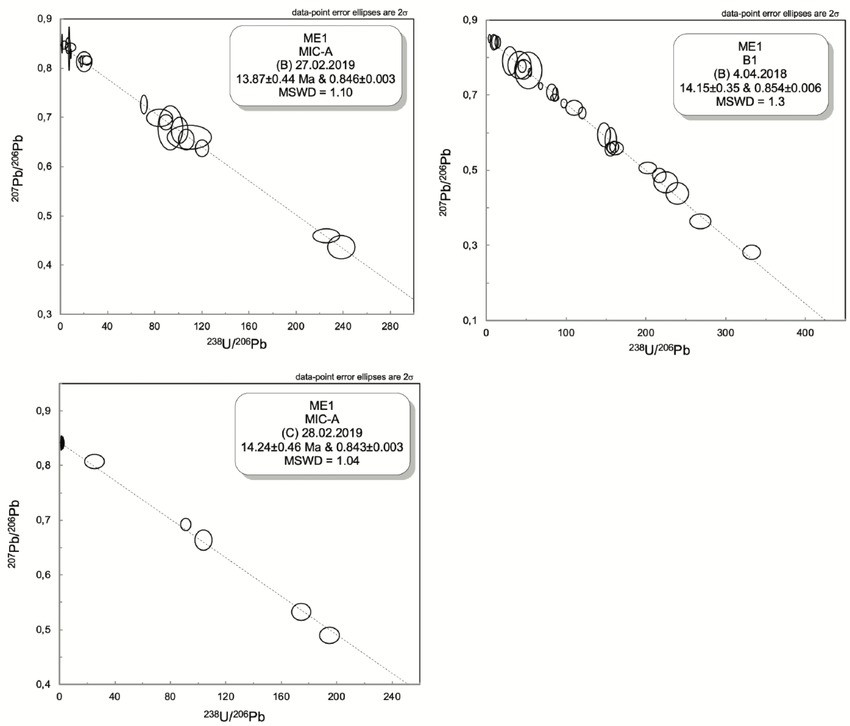

Figure E.1 $^{238}U/^{206}Pb$ *versus* $^{207}Pb/^{206}Pb$ Tera-Wasserburg Concordia diagrams and corresponding absolute ages for the Adlersberg bioherm sample (ME1). Dashed lines represent the isochrons. Ellipses represent the 'n' spot analyses and corresponding isotope ratios obtained. All absolute ages are reported with 2σ confidence.

Data repository F

Figure F.1. $^{238}U/^{206}Pb$ *versus* $^{207}Pb/^{206}Pb$ Tera-Wasserburg Concordia diagrams and corresponding absolute ages for the Hainsfarth bioherm sample (HAB2B6). Dashed lines represent the isochrons. Ellipses represent the 'n' spot analyses and corresponding isotope ratios obtained. All absolute ages are reported with 2σ confidence.

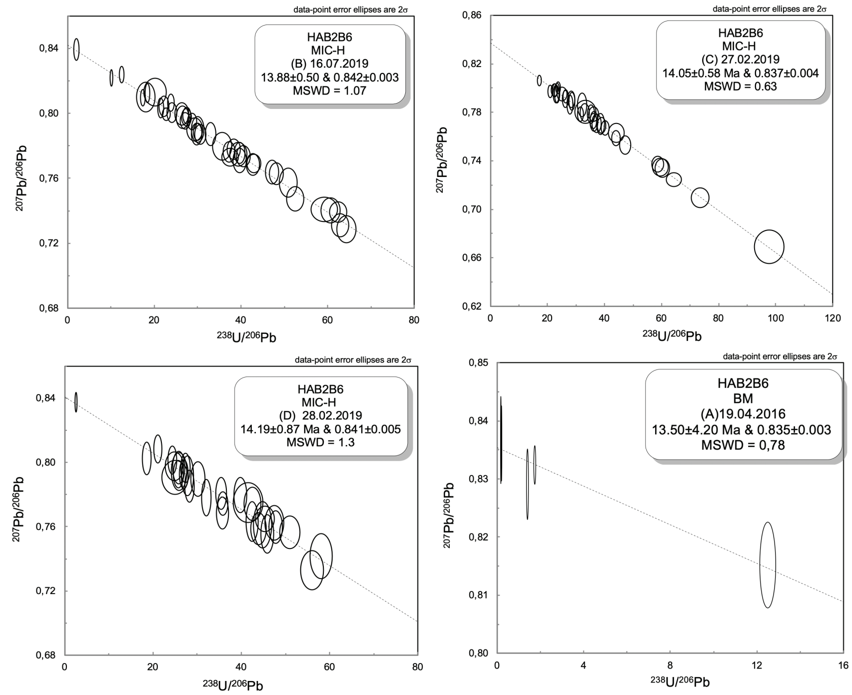

Data repository G

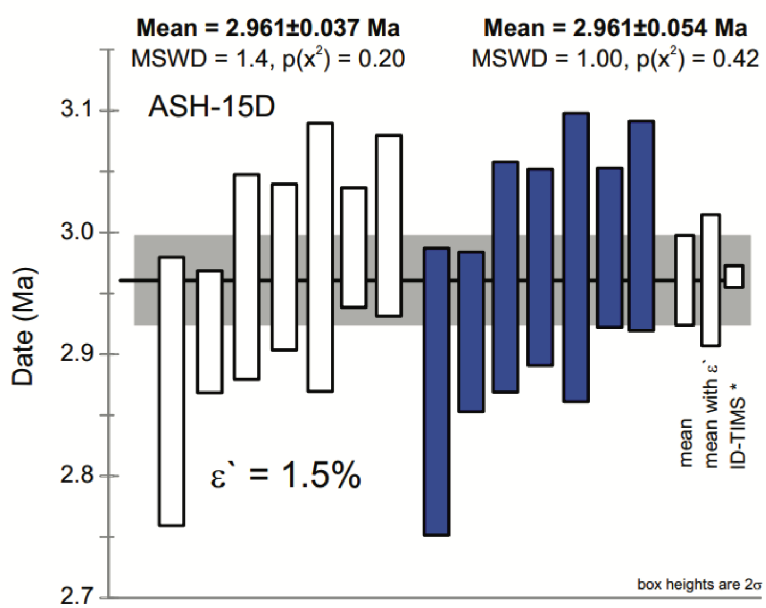

Figure G.1

Sorted intercept ages with 2σ uncertainty for ASH-15D (white; n_w = 7, MSWD = 1.4) analysed over a period of about 3 years (2016 to 2019) used to estimate the long-term excess of variance (ε`) of 1.5%. Data to the right (blue) includes the excess of variance propagated by quadratic addition. Also presented is the superpopulation mean with ε` and reference age from ID-TIMS (Nuriel et al., 2020).

References

Arp, G., Kolepka, C., Simon, K., Karius, V., Nolte, N., Hansen, B. T., 2013. New evidence for persistent impact-generated hydrothermal activity in the Miocene Ries impact structure, Germany. Meteorit. Planet Sci. 45 (12), 2491–2516. https://doi.org/10.1111/maps.12235.

Arp, G., Kolepka, C., Simon, K., Karius, V., Nolte, N., Hansen, B. T., 2013. New evidence for persistent impact-generated hydrothermal activity in the Miocene Ries impact structure, Germany. Meteorit. Planet Sci. 45 (12), 2491–2516. https://doi.org/10.1111/maps.12235.

Buchner, E., Schwarz, W. H., Schmieder, M., Trieloff, M., 2010. Establishing a 14.6 ± 0.2 Ma age for the Nördlinger Ries impact (Germany)—A prime example for concordant isotopic ages from various dating materials. Meteorit. Planet. Sci. 45 (4). https://doi.org/10.1111/j.1945-5100.2010.01046.x.

Buchner, E. & Schmieder, M. 2013. Das Ries–Steinheim-Ereignis – Impakt in eine miozäne Seen- und Sumpflandschaft—the Ries–Steinheim event – impact into a Miocene swampy lakescape. Z. Deutsch. Geol. Ges. 164, 459–470 (2013).

Füchtbauer, H., von der Brelie, G., Dehm, R., Förstner, U., Gall, H., Höfling, R., Hoefs, J., Hollerbach, A., Hufnagel, H., Jankowski, B., Jung, W., Malz, H., Mertes, H., Rothe, P., Salger, M., Wehner, H., Wolf, M., 1977. Tertiary lake sediments of the Ries, research borehole Nördlingen 1973—A summary. 75, 13-19. Geol. bavarica. DOI

Hilgen, F. J., Lourens, L. J., van Dam, J. A., 2012. The Neogene Period, in: Gradstein, F., Ogg, J., Schmitz, M. & Ogg, G. (Eds). The Geological Time Scale 2012. Elsevier, Amsterdam. https://doi.org/ 10.1016/B978-0-444-59425-9.00029-9.

Jankowski B., 1977. Die Postimpakt-Sedimente in der Forschungsbohrung Nördlingen 1973. *Geol. Bavarica.* 75, 21– 36.

Muttik, N., Kirsimäe, K., Newsom, H. E., Williams, L. B. 2011. Boron isotope composition of secondary smectite in suevites at the Ries crater, Germany: Boron fractionation in weathering and hydrothermal processes. Earth and Planetary Science Letters, 310, 244–251. https://doi.org/10.1016/j.epsl.2011.08.028

Nuriel, P., Wotzlaw, J., Ovtcharova, M., Vaks, A., Stremtan, C., Šala, M., Roberts, N. M. W., Kylander-Clark, A. R. C., 2020, in review. The use of ASH-15 flowstone as a matrix-matched reference material for laser-ablation U-Pb geochronology of calcite. Geochronology Discuss. https://doi.org/10.5194/gchron-2020-22.

Pohl, V. J. 1977. Paläomagnetische und gesteinsmagnetische Untersuchungen an den Kernen der Forschungsbohrung Nördlingen 1973. Geologica Bavarica 75, 328-348.

Pohl, J., Poschlod, K., Reimold, W. U., Meyer, C., Jacob, J., 2010. Ries crater, Germany: The Enkingen magnetic anomaly and associated drill core SUBO 18. In: Roger, L., Gibson, L., Reimold, W. U. (Eds.), Large Meteorite Impacts and Planetary Evolution IV, https://doi.org/10.1130/2010.2465(10).

Rocholl, A., Böhme, M., Gilg, H. A., Pohl J., Schaltegger, U., Wijbrans, J. 2018. Comment on ‘‘A high-precision $^{40}Ar/^{39}Ar$ age for the Nördlinger Ries impact crater, Germany, and implications for the accurate dating of terrestrial impact events” by Schmieder et al. (Geochim. et Cosmochim. Acta 220 (2018) 146–157). Geochim. et Cosmochim. Acta. 238, 599–601. https://doi.org/10.1016/j.gca.2018.05.018

Rocholl, A., Schaltegger, U., Gilg, H. A., Wijbrans, J., Böhme, M., 2017. The age of volcanic tuffs from the Upper Freshwater Molasse (North Alpine Foreland Basin) and their possible use for tephrostratigraphic correlations across Europe for the Middle Miocene. Int. J. Earth Sci. 107 (2), 387-407. https://doi.org/10.1007/s00531-017-1499-0.

Schmieder, M., Kennedy, T., Jourdan, F., Buchner, E., Reimold, W.U., 2018a. A high-precision $^{40}Ar/^{39}Ar$ age for the Nördlinger Ries impact crater, Germany, and implications for the accurate dating of terrestrial impact events. Geochim. Cosmochim. Acta. 220, 46-157. https://doi.org/10.1016/j.gca.2017.09.036.

Schmieder, M., Kennedy, T., Jourdan, F., Buchner, E., Reimold, W. U., 2018b. Comment on “A high-precision $^{40}Ar/^{39}Ar$ age for the Nördlinger Ries impact crater, Germany, and implications for the accurate dating of terrestrial impact events." By Schmieder et al. (Geochim. Cosmochim. Acta. 2018). 238, 599-601. https://doi.org/10.1016/j.gca.2018.05.018.

Schwarz, H. W., Hanel, M., Trieloffet, M. 2020. U-Pb dating of zircons from an impact melt of the Nördlinger Ries crater. Meteoritics & Planetary Science 55, Nr 2, 312–325. https://doi.org/ 10.1111/maps.13437.

Stöffler, D., Artemieva, N. A., Wünnemann K., Reimold, W. U., Jacob, J., Hansen B. K., Summerson, I. A. T., 2013. Ries crater and suevite revisited—Observations and modeling Part II: Modeling. *Meteorit. Planet. Sci.* 48 (4), 590-627. https://doi.org/10.1111/maps.12086.